

So long Kolmogorov: the forward and backward turbulence cascades in a supernovae-driven, multiphase interstellar medium

JAMES R. BEATTIE^{†,*} ^{1,2,3} ANNE NOER KOLBORG^{*} ³ ENRICO RAMIREZ-RUIZ ³ AND CHRISTOPH FEDERRATH ⁴

¹*Department of Astrophysical Sciences, Peyton Hall, Princeton University, Princeton, NJ 08544, USA*

²*Canadian Institute for Theoretical Astrophysics, University of Toronto, 60 St. George Street, Toronto, ON M5S 3H8, Canada*

³*Department of Astronomy and Astrophysics, University of California, Santa Cruz, 1156 High Street, Santa Cruz, CA 96054*

⁴*Research School of Astronomy and Astrophysics, Australian National University, Canberra, ACT 2611, Australia*

ABSTRACT

The interstellar medium (ISM) of disk galaxies is turbulent, and yet the fundamental nature of ISM turbulence, the energy cascade, is not understood in detail. In this study, we use high-resolution simulations of a hydrodynamical, gravitationally stratified, supernova (SNe)-driven, multiphase ISM to probe the nature of a galactic turbulence cascade. Through the use of kinetic energy flux transfer functions split into interactions between compressible \mathbf{u}_c and incompressible \mathbf{u}_s modes, we show that there exists a large-to-small-scale cascade in both \mathbf{u}_c and \mathbf{u}_s when mediated by an additional \mathbf{u}_s mode. But the \mathbf{u}_s cascade is highly non-local. Moreover, there is a \mathbf{u}_c mediated component of the \mathbf{u}_s cascade that proceeds in the opposite direction – an inverse cascade from small-to-large scales. The cascade feeds flux into scales well beyond the gaseous scale height, energizing the winds and fueling the direct cascades. Both the strongly non-local and the inverse \mathbf{u}_s cascades happen on scales that have a power law \mathbf{u}_s energy spectrum, highlighting how degenerate the spectrum is to the true underlying physical processes. We directly show that the inverse cascade comes from \mathbf{u}_s modes interacting with expanding SNe remnants (SNRs) and that \mathbf{u}_s modes are generated to leading order via baroclinic, highly corrugated cooling layers between warm ($T \lesssim 10^4$ K) and hot ($T \gg 10^4$ K) gas in these SNRs. Finally, we outline a complete phenomenology for SNe-driven turbulence in a galactic disk, estimate a 10^{-16} G Biermann field generated from SNR cooling layers, and highlight the strong deviations that SNe-driven turbulence has from the conventional Kolmogorov model.

Keywords: turbulence, hydrodynamics, ISM: kinematics and dynamics, galaxies: ISM, galaxies: structure

1. INTRODUCTION

The interstellar medium (ISM) of our Galaxy is turbulent, boasting hydrodynamical Reynolds numbers, $Re = UL/\nu$, between $\sim 10^2$ in the hot ($T > 10^6$ K) ionized medium, to $\sim 10^9$ in the cold ($T = 10$ K) molecular medium (Mac Low 1999; Krumholz 2015; Ferrière 2020), where U is characteristic velocity, L the system size scale, and ν the kinematic viscosity. Turbulence plays a diverse set of roles in the ISM, from regulating the star formation rate (Klessen et al. 2000; Krumholz &

McKee 2005; Hennebelle & Chabrier 2008; Hennebelle & Iffrig 2014; Federrath & Klessen 2012; Burkhardt 2018; Hennebelle et al. 2024) and modifying the initial mass function of stars (Nam et al. 2021; Mathew et al. 2023), to mixing metals (Krumholz & Ting 2018; Kolborg et al. 2022, 2023; Sharda et al. 2024) and generating and maintaining dynamically relevant magnetic fields (Schekochihin et al. 2002; Federrath et al. 2011; Schober et al. 2012, 2015; Xu & Lazarian 2016; Seta & Federrath 2022; Kriel et al. 2022, 2023; Beattie et al. 2023b,a). However, the exact origin of the turbulence is still an open question in ISM physics (e.g., Krumholz & Burkhardt 2016).

There is sufficient energy from supernova (SNe) alone to drive the turbulence to a steady state within our own Galaxy (Beck et al. 1996; Elmegreen & Scalo 2004; Hennebelle & Iffrig 2014; Padoan et al. 2016; Girichidis

Corresponding author:

[†]James R. Beattie: james.beattie@princeton.edu;

* these authors made equal contributions and should be deemed as joint first authors for the publication.

et al. 2016; Chamandy & Shukurov 2020; Bacchini et al. 2020), and maintain the multiphase structure (McKee & Ostriker 1977; Fielding et al. 2020; Guo et al. 2024), but the details of exactly how SNe, detonated on small scales, ℓ can facilitate an energy cascade from large-to-small scales, $L > \ell$, are quantitatively unknown. The large-to-small “direct” cascade, derived through Kolmogorov (1941)’s 4/5 law, is one of the few exact results in incompressible, homogeneous, isotropic turbulence. It reads,

$$\langle \delta u^3 \rangle_\ell = -\frac{4}{5}\varepsilon\ell \iff \nabla_\ell \cdot \langle \delta u^2 \delta \mathbf{u} \rangle_\ell = -4\varepsilon, \quad (1)$$

where $\langle \dots \rangle_\ell$ is the average over ℓ , $\delta \mathbf{u} = \mathbf{u}(\mathbf{r} + \boldsymbol{\ell}) - \mathbf{u}(\mathbf{r}) = \mathbf{u}' - \mathbf{u}$ is the velocity increment, and ε is the energy flux, which on the system scale is simply $\varepsilon \sim U^3/L$. We have also used the differential version of the expression as derived in Monin & Iaglom (1975) and recited in Banerjee & Galtier (2017), where the left-hand side of this equation is the kinetic energy flux on the scale ℓ , and because the right-hand side is negative, this implies that the flux acts like a converging ($\nabla \cdot \mathbf{u} < 0$) flow, moving down from large L to small ℓ . Indeed, Equation 1 was extended to homogeneous, compressible turbulence by Ferrand et al. (2020),

$$\nabla_\ell \cdot \langle \bar{\delta} \rho \delta u^2 \delta \mathbf{u} \rangle_\ell - \frac{1}{2} \langle (\rho \theta' + \rho' \theta) \delta u^2 \rangle_\ell = -4\varepsilon, \quad (2)$$

where ρ is the mass density, $\theta = \nabla \cdot \mathbf{u}$ and $\bar{\delta} \rho = (\rho' + \rho)/2$. Clearly, this means that ε can now change sign, based on whether or not the energy flux from the more classical cascade $\nabla_\ell \cdot \langle \bar{\delta} \rho \delta u^2 \delta \mathbf{u} \rangle_\ell$, is larger or smaller than the energy flux coupled to the dilatations and compressions, $\langle (\rho \theta' + \rho' \theta) \delta u^2 \rangle_\ell / 2$. One of the key goals of this paper is to understand how the flow of energy works in supernova-driven turbulence, which we will not explore through these exact relations, but instead energy flux transfer functions that allow us to directly probe the sign of ε .

Certainly, as we already showed in Equation 1 and Equation 2, the energy spectrum alone is insufficient to understand the fundamental nature of a turbulent plasma. This is already well-known, and we have to seek statistical tools that go beyond simply measuring Fourier amplitudes (see recent review Burkhart 2021). To make the reason why this is true clear, consider the following case. Kolmogorov (1941)-type turbulence has $\varepsilon = \text{const.}$ energy flux exchange between the k modes, and the energy is transported down a cascade with $u^2(k) \sim k^{-5/3}$, where $\varepsilon > 0$, as shown by Equation 1. However, in two-dimensional turbulence (or quasi-two-dimensional, which may be realized in a strongly stratified or magnetized limit) has the same $u^2(k) \sim k^{-5/3}$

spectrum as in Kolmogorov (1941), but with $\varepsilon < 0$ with a cascade moving from small ℓ to large ℓ (e.g., Kraichnan 1967; Boffetta & Ecke 2012), immediately showing that the spectrum alone is a degenerate statistic for understanding the nature of turbulence in a fluid. Padoan et al. (2016) showed that indeed the energy spectrum from SNe-driven turbulence in a triply-periodic box looks correct, in that the spectrum looks like the spectrum we get from local turbulent boxes, even with $u^2(k) \sim k^{-5/3}$. But, as we highlight above, this does not mean that Kolmogorov (1941) is at play.

Kolmogorov (1941)-type turbulence is regularly invoked (or at least broadly imagined) for the ISM in our own Galaxy (e.g., Armstrong et al. 1995; Elmegreen & Scalo 2004; Falceta-Gonçalves et al. 2014; Hopkins et al. 2021; Nandakumar & Dutta 2023), but what if supernova-driven turbulence is different? It could be Batchelor (1959)-like instead, where low- k turbulent modes couple ε non-locally to all scales (e.g., Adkins & Schekochihin 2018), and the self-similarity of the energy spectrum is not a repercussion from a local cascade at all? Of course, Burgers (1948)-type turbulence is also regularly invoked (Federrath 2013; Krumholz 2015; Federrath et al. 2021; Beattie et al. 2024; Cernetic et al. 2024), which should not have a cascade at all because it is simply the spectrum one gets from Fourier transforming a velocity discontinuity and dumping ε on all scales. The key point is that ε is what we need to measure as a function of k to distinguish between these different turbulent models.

For decades, turbulent boxes have been used as local models of the ISM (e.g., Stone et al. 1998; Burkhart et al. 2020; Federrath et al. 2021; Hu et al. 2022; Kempski et al. 2023; Kriel et al. 2023; Fielding et al. 2023; Beattie et al. 2024, and many more), usually employing Fourier space driving, where momentum is directly injected on low k modes (large scales), and in the absence of kinetic and magnetic helicity (e.g., Waleffe 1992; Alexakis 2017; Plunian et al. 2020), a self-consistent direct cascade is formed, albeit over a limited range of scales (see Beattie et al. 2024 for the currently highest resolution turbulence box in the world, with $\text{Re} \gtrsim 10^6$, resolving a few orders of magnitude of length scales within the turbulent cascade). However, if the ISM is energized by SNe on the small scales, it is not clear how well these local simulations faithfully represent the ISM. We aim to address this question throughout the study, starting with the spectrum, energy fluxes, and then finishing with the generation of vorticity.

In this study, we directly explore how the kinetic energy flux, $\varepsilon \sim U^3/L$ and turbulent cascade $E_{\text{kin}}(k) \sim k^{-\alpha}$, work in stratified supernova-driven turbulence,

with a time-dependent chemical network that provides a multiphase ISM. To do this, we use shell-to-shell kinetic energy flux transfer functions, (e.g., Grete et al. 2017a, 2020, 2021, 2023) generalized to calculate compressible and incompressible mode interactions. Previous works have performed detailed and important analyses of supernova-driven energetics (Martizzi et al. 2016; Li et al. 2020; Mohapatra & Quataert 2024). However, no study has performed them with a k mode-by-mode focus, making our study rather unique and highly illuminating. We neglect magnetic fields and galactic rotation to focus solely on the impact of the supernova-driven turbulence, with a previously utilized setup (Martizzi et al. 2016; Kolborg et al. 2022, 2023) at much higher grid resolutions of up to $1,024^3$. This allows us to fully characterize the effect of SNe-driven turbulence at a level of detail that has never been done before.

This study is organized as follows. In Section 2 we discuss the gravito-hydrodynamical fluid model, initial and boundary conditions, SNe-driving prescription, cooling function and phase structure, our key dimensionless parameters, and reaching stationarity in a SNe-driven ISM. In Section 3 we define the Helmholtz decomposition that we perform on our velocity field, and discuss the qualitative behavior of each component. In Section 4 we define the velocity power spectrum and show the results from the cylindrically integrated velocity spectrum, separated into compressible and incompressible modes and cylindrical coordinates. In Section 5 we define and discuss results of Helmholtz decomposed shell-to-shell energy flux transfer functions, building on the methods from Grete et al. (2017a, 2020, 2021, 2023), focusing on like-mode interactions, the emergence of an inverse cascade, and time variability in the standard incompressible, Kolmogorov (1941)-type, cascade. In Section 6 we compute each of the source terms in the vorticity evolution equation, show that the baroclinic term dominates the generation of vorticity in this type of turbulence, and identify the main sources as fractal cooling layers embedded inside of expanding SNRs. We use our simulations to estimate how strong the Biermann magnetic field would be from the cooling layer, which is $\sim 10^{-16}$ G. Finally, in Section 7, we define an entire phenomenology for SNe-driven turbulence and how it may work in the disk of a galaxy, from the initial adiabatic expansion of the SNR to the energy flux of all different mode combinations. We focus on and highlight how compressible and incompressible modes both have different but vitally important roles in this type of turbulence, and further emphasize how vastly different SNe-driven turbulence ends up being compared to Kolmogorov.

2. NUMERICAL SIMULATIONS & METHODS

We model the ISM in a section of a disk galaxy, and the simulation parameters are chosen such that the resulting galaxy parameters are similar to those of the present-day Milky Way. In the following, we summarize the fluid model, the chosen model parameters, and some of the basic statistics from the simulation, including the phase structure.

2.1. Multiphase, supernova-driven, gravito-hydrodynamical fluid model

We model sections of a galaxy disk based on the setup of Martizzi et al. (2016). For our ISM simulations, we solve the three-dimensional, compressible Euler equations in a static gravitational field with mass, momentum and energy sources from stochastic supernova events (\sim point sources of extreme mass, momentum and energy) using the RAMSES code (Teyssier 2002) employing the Monotonic Upstream-centered Scheme for Conservation Laws (MUSCL) scheme and HLLC Riemann solver. The model is

$$\frac{\partial \rho}{\partial t} + \nabla \cdot (\rho \mathbf{u}) = \dot{n}_{\text{SNe}} M_{\text{ej}}, \quad (3)$$

$$\frac{\partial \rho \mathbf{u}}{\partial t} + \nabla \cdot (\rho \mathbf{u} \otimes \mathbf{u} + P \mathbb{I}) = -\rho \nabla \phi + \dot{n}_{\text{SNe}} \mathbf{p}_{\text{SNe}}(Z, n_{\text{H}}), \quad (4)$$

$$\begin{aligned} \frac{\partial \rho e}{\partial t} + \nabla \cdot [\rho (e + P) \mathbf{u}] = & -n_{\text{H}}^2 \Lambda - \\ & \rho \mathbf{u} \cdot \nabla \phi + \dot{n}_{\text{SNe}} \left[E_{\text{th,SNe}}(Z, n_{\text{H}}) + \frac{p_{\text{SNe}}^2(Z, n_{\text{H}})}{2(M_{\text{ej}} + M_{\text{swept}})} \right], \end{aligned} \quad (5)$$

$$e = \epsilon + \frac{u^2}{2}, \quad P = \frac{2}{3} \rho e, \quad (6)$$

where \otimes is the tensor product, such that $\mathbf{u} \otimes \mathbf{u} = u_i u_j$. \mathbf{u} is the gas velocity, ρ is the gas density. $\nabla \phi$ describes the static gravitational potential, $\partial_t \nabla \phi = 0$, the details of this potential are described in Section 2.1.1. P is the scalar pressure, and \mathbb{I} is the unit tensor, δ_{ij} . ρe is the total energy composed of both the kinetic energy of the gas, $\rho u^2/2$ and the internal energy, ϵ . \dot{n}_{SNe} is the volumetric rate of SNe, \mathbf{p}_{SNe} , M_{ej} , and $E_{\text{th,SNe}}$ are the radial momentum, the mass of the ejecta, and the thermal energy of each SNe. M_{swept} is the mass of ISM material swept up by the SNe shock wave. Z is the metallicity of the ambient medium. Λ is the cooling function, which encompasses both the heating and cooling terms; the underlying physical model is discussed in Section 2.1.4. Finally, n_{H} is the number density of hydrogen (atomic and ionized).

A variety of metals are injected into the medium from the SNe, see Appendix in Kolborg et al. (2022) for more

Table 1. Main simulation parameters and derived quantities.

Galaxy model	$\langle \rho \rangle_V$ [g cm ⁻³]	L [pc]	ℓ_0 [pc]	t_0 [Myr]	$\langle u^2 \rangle_V^{1/2}$ [km/s]	\mathcal{M}	$\ell_{\text{cor},\parallel}$ [pc]	$\ell_{\text{cor},\perp}$ [pc]	N_{grid}^3
(1)	(2)	(3)	(4)	(5)	(6)	(7)	(8)	(9)	(10)
MW_1024	7.85×10^{-25}	1,000	85 ± 6	2.9 ± 0.7	28 ± 6	1.75 ± 0.05	$(35 \pm 3) \times 10^1$	$(29 \pm 2) \times 10^1$	$1,024^3$
MW_512	7.84×10^{-25}	1,000	86 ± 5	2.3 ± 0.5	37 ± 8	1.82 ± 0.02	$(35 \pm 2) \times 10^1$	$(29 \pm 2) \times 10^1$	512^3
MW_256	7.83×10^{-25}	1,000	88 ± 5	2.7 ± 0.6	32 ± 7	1.80 ± 0.05	$(36 \pm 2) \times 10^1$	$(32 \pm 2) \times 10^1$	256^3

Notes. Column (1): Simulation label. Column (2): volume-weighted mean gas density. Column (3): the length of the cubic simulation domain. Column (4): the effective scale height of the gaseous disk fit by an empirical model in the steady state. Column (5): the turbulent turnover time at the gaseous scale height, column (4), as shown in Equation 15. Column (6): the root-mean-squared (rms) turbulent (rest-frame) velocity. Column (7): the volume-weighted turbulent Mach number, as shown in Equation 14. Column (8): the correlation scale of the total velocity fluctuations parallel to $\nabla\phi$, computed from the power spectrum. Column (9): the same as column (8) but for the total velocity fluctuations perpendicular to $\nabla\phi$. Column (10): the total number of cells used in the grid discretisation of the simulation. All statistics in the table are averaged over $10t_0$ in the statistically steady state shown in Figure 3.

details. Each metal, Z_i , follows the passive scalar transport equation,

$$\frac{\partial Z_i}{\partial t} + \mathbf{u} \cdot \nabla Z_i = \mathcal{S}_{\text{SNe}}, \quad (7)$$

where \mathcal{S}_{SNe} is the source of metals from SNe. For further, detailed discussion of, e.g., Z_i yields, we refer to Kolborg et al. (2022). Further details of the SNe driving are discussed in Section 2.1.3. The Z composition of the medium is utilized by Λ , which then contributes to determining the local thermodynamic properties of the plasma.

We choose a cubic simulation domain of side length, $L = 1,000$ pc, with periodic boundary conditions on the four sides perpendicular to the disk midplane and outflow boundaries on the top and bottom boundaries. The domain is discretized using a regular Cartesian grid of up to $N_{\text{grid}} = 1024$ cells for each L . For second-order spatial reconstruction methods such as the one used to solve our model, the numerical diffusive effects influence $\approx 10 dx$ (Malvadi Shivakumar & Federath 2023; Beattie et al. 2023a), where $dx = L/N_{\text{grid}}$, which means that at $N_{\text{grid}} = 1024$ we properly resolve roughly $10 \text{ pc} \lesssim \ell \lesssim 1,000 \text{ pc}$ in our simulations. This study includes three simulations with exactly the same fluid parameters, but with resolutions of $N_{\text{grid}} = 256$ to $N_{\text{grid}} = 1024$ for convergence tests. The parameters of each of the runs are summarized in Table 1.

2.1.1. Gravitational potential

The simulations employ a static gravitational potential, $\phi(z)$, with stellar disk of scale height z_0 and surface density Σ_* and a spherical dark matter halo of density ρ_{halo} ,

$$\phi(z) = 2\pi G \Sigma_* \left(\sqrt{z^2 + z_0^2} - z_0 \right) + \frac{2\pi G \rho_{\text{halo}}}{3} z^2 \quad (8)$$

with the accelerations $2\pi G \Sigma_* z / \sqrt{z^2 + z_0^2}$ due to the disk component and $(4/3)\pi G \rho_{\text{halo}} z$ due to the halo (Kuijken & Gilmore 1989). The stellar scale height, z_0 , and the halo density ρ_{halo} are chosen to match the Milky Way model in Martizzi et al. (2016, ; see Table 1, MW model). Likewise, we fix Σ_* to Σ_{gas} by the gas fraction $f_{\text{gas}} = \Sigma_{\text{gas}}/\Sigma_* = 0.088$, which is chosen to mimic that of the present-day Milky Way within the Solar neighborhood (MW; McKee et al. 2015). With these parameters, the gravitational potential has a scale height, $z_{\text{eff}} = 180$ pc (Kolborg et al. 2023).

2.1.2. Initial conditions

The simulation is initialized at $t = t_{\text{init}}$ in hydrostatic equilibrium, where we use $\rho(z, t_{\text{init}}) = \rho_0 \exp\{-f\phi(z)\}$ and $P(z, t_{\text{init}})/k_B = T_0 \rho(z, t_{\text{init}})/(\mu m_{\text{H}})$, where k_B is the Boltzmann constant, $\mu = 0.6$ is the mean molecular weight, m_{H} is the mass of hydrogen, and $\rho_0 = 2.1 \times 10^{-24} \text{ g cm}^{-3}$ is chosen such that the gas surface density, $\Sigma_{\text{gas}} = 5 M_{\odot}/\text{pc}^2$, is similar to that of the present-day solar neighborhood value (McKee et al. 2015, see also Martizzi et al. 2016), and similarly for the initial metallicity of the simulation $Z = Z_{\odot}$. The constant in the exponential ρ atmosphere is $f = m_{\text{H}}\mu/(k_B T_0)$, where $T_0 = 12,891 \text{ K}$ is the constant initial temperature. In addition, through T_0 and ρ_0 , we define a midplane pressure of $P_0/k_B = 1.6 \times 10^4 \text{ K cm}^{-3} = T_0 \rho_0/(\mu m_{\text{H}})$. The gas velocity is initialized $|\mathbf{u}| = 0$, without initial velocity perturbations.

2.1.3. Supernova driving

Energy, mass and momentum are injected into the medium via core collapse SNe detonations. The injection is modeled using the sub-grid model in Martizzi et al. (2015). The model takes into account ambient ρ and Z in the local medium where a SNe detonates and partitions the total energy, $E_{\text{SNe}} = 10^{51} \text{ erg}$ into (radial

momentum, \mathbf{p}_{SNe} and thermal energy, $E_{\text{th,SNe}}$. Each SNe ejects $M_{\text{ej}} = 6.8 M_{\odot}$ new material, including Z_i , into the ISM, and as the shock wave expands through the medium it continuously sweeps material M_{swept} . M_{ej} , \mathbf{p}_{SNe} and $E_{\text{th,SNe}}$ are deposited over a region of size $\ell_{\text{inj}} = 2 dx$, fixed for all N_{grid} . This means that the SNe are detonated on progressively smaller physical scales as we go to higher N_{grid} . This is, of course, a degree of freedom, in that we could have fixed ℓ_{inj} to a physical scale, but in reality the SNe will be detonated on scales well below any of the resolved scales ($dx \sim 1$ pc at the highest resolutions), so this is indeed well justified, but does mean our energy injection scale shifts as we go to higher N_{grid} . We perform convergence studies on the spectra in [Appendix E](#) to ensure that nothing peculiar happens to the turbulence between the different N_{grid} . The volumetric rate of SNe, \dot{n}_{SNe} is given,

$$\dot{n}_{\text{SNe}} = \frac{\dot{\Sigma}_{*}}{2z_{\text{eff}} 100 M_{\odot}}, \quad (9)$$

where $\dot{\Sigma}_{*} \propto \Sigma_{\text{gas}}^{1.4}$ is the surface density of star formation ([Kennicutt 1998; Kennicutt et al. 2007](#)). This results in one SNe occurring for every $100 M_{\odot}$ stars formed.

The positions of a SNe is chosen at random within a fixed volume. Parallel to the gravitational potential, the distribution function or SNe positions is,

$$p(z) = \begin{cases} 1/(2z_{\text{eff}}), & |z| \leq z_{\text{eff}}, \\ 0, & |z| > z_{\text{eff}}, \end{cases} \quad (10)$$

i.e., the SNe have an equal probability of happening anywhere within $z \pm z_{\text{eff}}$ of the disk midplane and zero probability outside this region. In the perpendicular direction (i.e., in the disk plane) the SNe positions follow a uniform distribution. This is a very simple prescription, but we intend to explore other schemes in future works.

2.1.4. Heating and cooling

We employ a heating and cooling model to capture the multiphase nature of the ISM ([McKee & Ostriker 1977; Wolfire et al. 1995](#)). The model is based on the microphysical heating and cooling prescriptions studied in [Theuns et al. \(1998\)](#) and [Sutherland & Dopita \(1993\)](#). The cooling function Λ has both cooling \mathcal{C} and heating \mathcal{H} terms,

$$\Lambda(n_{\text{H}}, Z) = \mathcal{H}(n_{\text{H}}) - \mathcal{C}(n_{\text{H}}, Z). \quad (11)$$

The model solves a time-dependent chemical network consisting of HI, HII, HeI, HeII, HeIII and free electrons. The solution to this network forms the basis for computing \mathcal{H} and \mathcal{C} . Our heating term, \mathcal{H} is due solely to photoheating, which is the excess energy in free electrons

that have been ejected from HI, HeI and HeII atoms,

$$\mathcal{H} = (n_{\text{HI}}\epsilon_{\gamma\text{HI}} + n_{\text{HeI}}\epsilon_{\gamma\text{HeI}} + n_{\text{HeII}}\epsilon_{\gamma\text{HeII}}) / n_{\text{H}}^2, \quad (12)$$

where the photo-heating rates, ϵ_{γ} , are those reported in Table B4 of [Theuns et al. \(1998\)](#) and depend on the rate of photoionization by the background power-law UV spectrum, $J(\nu)$ (see Equation B11 of [Theuns et al. 1998](#)). The total cooling rate, \mathcal{C} , is given by

$$\mathcal{C} = \sum_{i=1}^{10} c_i(T, n_{\text{H}}) + c_{\text{metal}}(T, n_{\text{H}}, Z), \quad (13)$$

where we sum over each of five physical processes: collisional ionization (HI, HeI and HeII); recombination (HII, HeII, HeIII); dielectronic recombination (HeII); collisional excitation (HI and HeII); and, Bremsstrahlung (HII, HeII and HeIII). We use the rates from Appendix B1 of [Theuns et al. \(1998\)](#). However, our cooling model neglects the inverse Compton cooling term, which is included in the original [Theuns et al. \(1998\)](#) model. Furthermore, we supplement the [Theuns et al. \(1998\)](#) model with cooling due to metal line emission, c_{metal} , following the model from [Sutherland & Dopita \(1993\)](#). Z is sourced by the injection of metals from SNe, as we indicated in [Equation 7](#). As discussed in [Karpov et al. \(2020\)](#), SNe injection will not create a solar abundance pattern, and in reality, one needs many additional metal production channels, which we do not take into account in our model.

The total heating and cooling implemented in the code is shown in [Figure 1](#) at fixed density $n_{\text{H}} = 1 \text{ cm}^{-3}$ and solar metallicity. The thick black line is the total net-cooling, Λ , while the dash-dotted black line is photoheating, \mathcal{H} . The colored lines indicate the contributions to the cooling by each process modeled as indicated along the respective lines. At temperatures $10^4 \text{ K} \lesssim T \lesssim 10^8 \text{ K}$ cooling is dominated by metal line emission for $Z \approx Z_{\odot}$ and at $Z < Z_{\odot}$ collisional excitation and ionization dominate the cooling when $T \lesssim 10^6$. However, for $T \gtrsim 10^8 \text{ K}$ (and for $T \sim 10^7 \text{ K}$, for low Z) bremsstrahlung dominates the cooling function. Changes in n_{H} only result in significant changes to the total cooling at temperatures $T < 10^4 \text{ K}$ as shown by the gray line for $n_{\text{H}} = 10^{-3} \text{ cm}^{-3}$. In general, most of the cooling terms are truncated at $T \approx 10^4 \text{ K}$; therefore, the simulations do not self-consistently form a cold (or WNM) phase of the ISM via condensation, and any gas at $T \lesssim 10^4 \text{ K}$ is from the adiabatic expansion of SNRs. Additional cooling terms are unlikely to lead to significantly different results in our simulations because the cold gas would be poorly resolved, since we already expect numerical diffusion effects to influence ~ 10 pc,

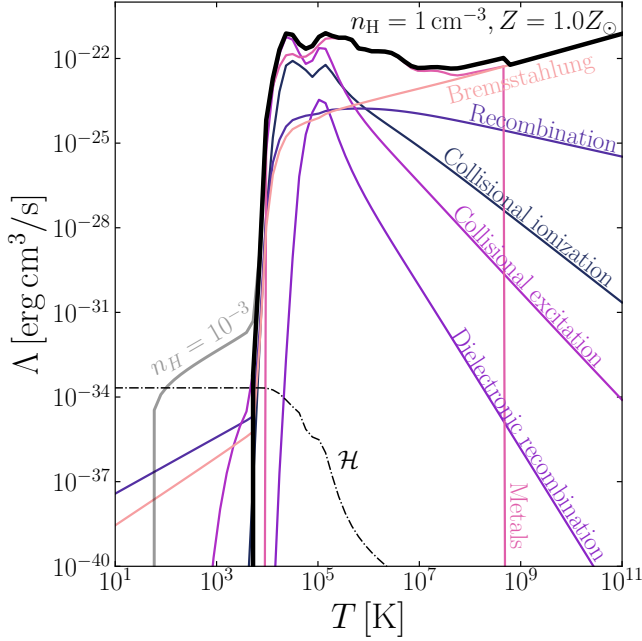


Figure 1. The heating and cooling curve we employ in our simulation. The black solid line is the total cooling, Λ , at $n_{\text{H}} = 1 \text{ cm}^{-3}$ and $Z = Z_{\odot}$. Each component of the total cooling is plotted for the same density and metallicity in colored lines, labeled by the associated physical process. The gray line is the total cooling at the indicated lower density, showing that the gas density only significantly influences the cooling at $T \lesssim 10^4 \text{ K}$. The black, dash-dotted line is the total photoheating, \mathcal{H} , at gas density $n_{\text{H}} = 1 \text{ cm}^{-3}$.

which is approximately the size-scale of the largest cold clumps (that can individually have $\text{Re} \sim 10^{10}$, but would be resolved with $\text{Re} \sim 1$ in our simulations; Ferrière 2020) in bistable simulations of turbulence boxes (Fielding et al. 2023). Hence, we focus on simulating the large-scale warm (WIM) and hot (HIM) phases of the ISM.

To more clearly understand how Λ translates into different ISM phases in our simulation, in Figure 2 we plot time-averaged phase diagrams of P/P_0 (top panel) and T/T_0 (bottom panel) as a function of ρ/ρ_0 . All parameters have been normalized by their initial midplane condition values (see Section 2.1.2 and Table 1), and we plot isotherms to help guide the eye. As expected, the impact of the drastic drop in cooling efficiency for $T \lesssim 10^4 \text{ K}$ is translated into both the P/P_0 - ρ/ρ_0 and T/T_0 - ρ/ρ_0 distribution functions by the build-up of probability density (i.e., the volume filling factor of the gas) around the $T = 10^4 \text{ K}$ isotherm. The most efficient mechanism for gas to cool below this $T \lesssim 10^4 \text{ K}$ is through adiabatic expansion caused by expanding SNRs, and we observe directly that the trajectory from the $T = 10^4 \text{ K}$ to the $T = 10^2 \text{ K}$ isotherm follows an adiabat, $P \propto \rho^\gamma$, which we plot in blue (where we use $\gamma = 5/3$ for a monoatomic

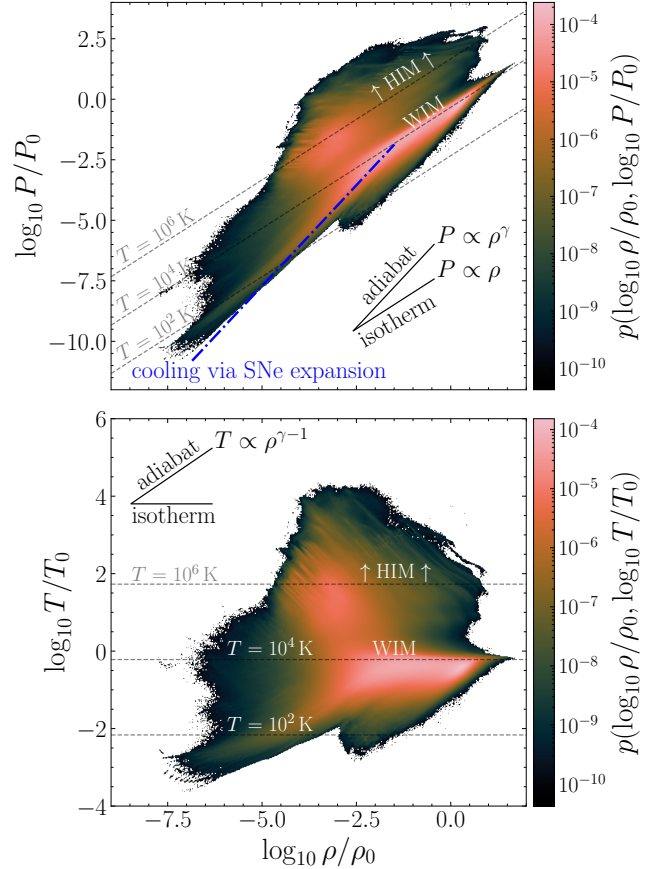


Figure 2. Two-dimensional, time-averaged pressure-density (top panel) and temperature-density (bottom panel) probability distribution functions, illustrating the presence of a multiphase ISM with a hot $T \geq 10^6 \text{ K}$ (HIM) and volume-filling warm phase $T \sim 10^4 \text{ K}$ (WIM), annotated on each of the panels. All parameters have been normalized by their initial midplane values, $\rho_0 = 2.1 \times 10^{-24} \text{ g cm}^{-3}$, $P_0/k_B = 1.6 \times 10^4 \text{ K cm}^{-3}$ and $T_0 = 12,891 \text{ K}$. We plot example adiabats $P \propto \rho^\gamma$ and isotherms $P \propto \rho$ in both panels. Due to the lack of explicit cooling to $T \leq 10^4 \text{ K}$ temperatures (see Figure 1), the $T \lesssim 10^4 \text{ K}$ gas is reached only through the adiabatic cooling from expanding SNe remnants, highlighted with a blue adiabat from $T \sim 10^4 \text{ K}$ to $T \sim 10^2 \text{ K}$ in the top panel. The distributions have been averaged over all realizations in the steady state (see Section 2.2).

gas). Indeed, we observe small volumes of the ISM (small probability densities) getting to $T \lesssim 10^2 \text{ K}$ via this mechanism.

2.2. Characteristic scales, dimensionless numbers and stationarity

In this section, we describe the characteristic velocities, length scales, and time scales of the simulation. We first calculate the (instantaneous) global average turbu-

lent Mach number,

$$\mathcal{M} = \left\langle \left(\frac{u}{c_s} \right)^2 \right\rangle_{\mathcal{V}}^{1/2}, \quad (14)$$

given by the ratio between the dispersion of the local nonthermal, turbulent (rest-frame) velocities $\langle u^2 \rangle_{\mathcal{V}}^{1/2}$ and thermal velocity dispersion, $\langle c_s^2 \rangle_{\mathcal{V}}^{1/2}$. Furthermore, it is useful to consider the measured scale height of the gaseous disk (rather than z_{eff} , which is the analytical steady state, not including SNe contributions) ℓ_0 , such that $\rho(z) \propto \exp(-|z|/\ell_0)$. With our cooling function, as well as the SNe detonation and turbulence, it makes the analytical equilibrium profile and ℓ_0 challenging to derive; hence, we resort to numerical means for computing this scale. We directly fit an exponential model to the steady state data and measure ℓ_0 , and then average it over time. From $\langle u^2 \rangle_{\mathcal{V}}^{1/2}$ and ℓ_0 we define the characteristic time scale of the simulation, the turbulent turnover time at ℓ_0 ,

$$t_0 = \frac{\ell_0}{\langle u^2 \rangle_{\mathcal{V}}^{1/2}}. \quad (15)$$

We will use \mathcal{M} , ℓ_0 and t_0 regularly throughout the study. This is, in many ways, analogous to the non-dimensionalizations used regularly in turbulence box simulations (e.g., Beattie et al. 2022b). We do, however, note that the ℓ_0 we compute above is not the outer scale of the turbulence, which we compute independently below in Section 4, directly from the velocity spectrum.

Because we are using a second-order spatial reconstruction method, we can directly estimate the hydrodynamical Reynolds number utilizing numerical dissipation relations in Malvadi Shivakumar & Federrath (2023). For our N_{grid} we get $\text{Re} \sim 10^4$ on the outer scale, which maps to the Re of the transonic, volume-filling WIM ($T \sim 10^4$ K) in our simulations. At these Re , we do resolve the HIM ($\text{Re} \sim 10^2$), which is relatively viscous because of the high temperatures, $T \sim 10^6$ K, and low electron densities ($n_e \sim 10^{-3}$), leading from the fact that $\text{Re} \propto n_e T^{-5/2}$ (Ferrière 2020). However, for the WIM, which is the volume-filling phase in our simulation, this is a few orders of magnitude away from a realistic Re , with $\text{Re} \sim 10^7$. However, at $\text{Re} \sim 10^4$ we will still have a turbulent warm phase, that ought to have at least some of the cascade resolved (indeed we see this is the case in Section 5), at least when we compare to turbulent box simulations with the same order spatial reconstruction method (e.g., Federrath 2013). Based on the required Re , to get a completely resolved WIM we would need to go to grid resolutions of $N_{\text{grid}} \gtrsim 10,000$ (as in Federrath et al. 2021 and Beattie et al. 2024) and

above, which would be an exciting direction for future work.

The early time in the simulation is characterized by relaxation from the initial conditions – as the gas cools it collapses in $\nabla\phi$; simultaneously, feedback from SNe turns on injecting mass, momentum and energy into the disk (Kolborg et al. 2022, 2023). These injections drive turbulence in the ISM and contribute to pressure support of the gas (via ∇u^2) in $\nabla\phi$. Eventually the disk settles into a statistically steady-state where

$$\langle \nabla \cdot (\rho \mathbf{u} \otimes \mathbf{u} + P\mathbb{I}) \rangle_{\mathcal{V}} = - \langle \rho \nabla \phi \rangle_{\mathcal{V}} + \langle \dot{n}_{\text{SNe}} \mathbf{p}_{\text{SNe}}(Z, n_H) \rangle_{\mathcal{V}}, \quad (16)$$

in which a stationary turbulent cascade forms, e.g., $\varepsilon_{\text{injection}} = \varepsilon_{\text{dissipation}}$ (Li et al. 2020), where $\varepsilon_{\text{injection}}$ is the flux from the SNe injection, and $\varepsilon_{\text{dissipation}}$ is the dissipated flux, which is both a function of Equation 12 and the numerical dissipation from the discretisation, which we discuss in detail in Section 4 and Section 5.

To determine when the stationary state is reached we plot the evolution of the volume-weighted \mathcal{M} in Figure 3. Volume-averaged over the entire ISM, we find $\mathcal{M} = 1.37 \pm 0.04$ in the steady state (and $\langle u^2 \rangle_{\mathcal{V}}^{1/2} = 28 \pm 6 \text{ km s}^{-1}$), consistent with the \mathcal{M} derived from observations of the volume-filling, warm-ionized medium in the ISM ($\mathcal{M} \approx 2$ Gaensler et al. 2011; Ferrière 2020; Gerrard et al. 2024). Compared to Fourier driven turbulent boxes (e.g., Federrath 2013; Beattie et al. 2022c), \mathcal{M} has many more intermittent events, associated with sudden intense detonations of SNe (Kolborg et al. 2022). However, the intensity of these fluctuations decreases as we go from $N_{\text{grid}} = 256$ to $N_{\text{grid}} = 1,024$, most likely due to the reduction of the volume-filling factor for the initial SNe seeds. In Section 5.5, we will later explore the effect (the time variability, not N_{grid}) that this has on the k space statistics, including the energy flux in the energy cascade. Using our exponential profile model, in this state we find $\ell_0 = 85 \pm 6 \text{ pc}$ for $N_{\text{grid}} = 1,024$, allowing us to derive $t_0 = 2.9 \pm 0.7 \text{ Myr}$. We list ℓ_0 , t_0 and for $\langle u^2 \rangle_{\mathcal{V}}^{1/2}$ all grid resolutions in Table 1, showing good agreement up to 1σ .

We identify a range of t/t_0 wherein the time-averaged \mathcal{M} no longer changes significantly for different time windows, $\langle \mathcal{M}(t) + \mathcal{M}(t + \Delta t) \rangle_{\Delta t} \approx 0$. This occurs at approximately $t/t_0 \gtrsim 27$, after the initial transient stage associated with reaching a new quasi-equilibrium, Equation 16. Throughout this study, we will average over realizations in $27 \lesssim t/t_0 \lesssim 37$ ($10t_0$ in the statistically steady state), indicated with the gray band in Figure 3. Compared to momentum driven turbulence in Fourier space, it takes roughly an order of magnitude longer in t/t_0 to reach a steady state (Beattie et al. 2022c,b). Of

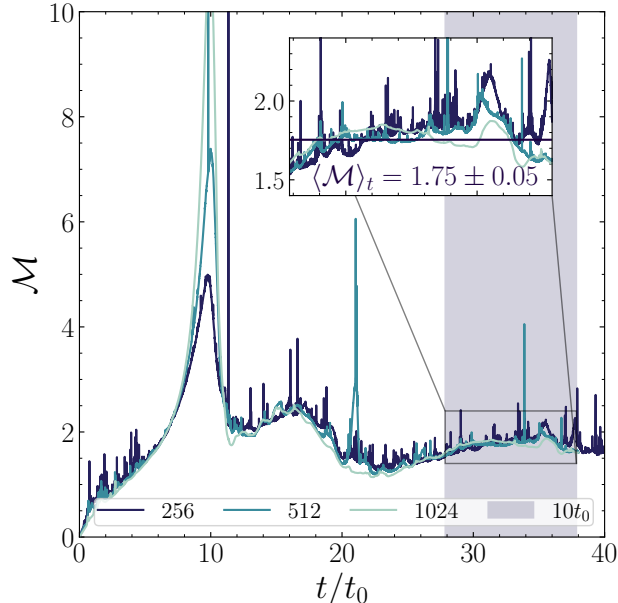


Figure 3. Evolution of the global, volume-weighted turbulent Mach number, \mathcal{M} (Equation 14), plotted as a function of the turbulent turnover time, $t_0 = 2.9 \pm 0.7$ Myr (Equation 15), with each color indicating a different linear grid resolution. The turbulence reaches a steady state for $t \gtrsim 27 t_0$. The shaded region marks the steady state over which all of the results in this study are taken, unless explicitly stated otherwise, for which the ISM is at $\mathcal{M} \approx 1.8$, i.e., transonic, consistent with radio observations of the Milky Way’s ISM (Gaensler et al. 2011).

course, this could be reduced by finding better initial conditions that capture Equation 16 more accurately, specifically the enhancement in the scale-height from $\langle \dot{n}_{\text{SNe}} p_{\text{SNe}}(Z, n_{\text{H}}) \rangle_{\mathcal{V}}$.

3. VELOCITY STRUCTURE & HELMHOLTZ DECOMPOSITION

Critical to our analysis of the turbulent cascade is the nature of the velocity modes. We decompose \mathbf{u} into compressible \mathbf{u}_c ($|\nabla \times \mathbf{u}_c| = 0$) and incompressible \mathbf{u}_s ($\nabla \cdot \mathbf{u}_s = 0$) modes, using a Helmholtz decomposition of the field, such that,

$$\mathbf{u} = \mathbf{u}_c + \mathbf{u}_s, \quad \text{and} \quad \mathbf{u}_c \cdot \mathbf{u}_s = 0. \quad (17)$$

We do this in Fourier space, where

$$\mathbf{u}_c(\ell) = \int d\mathbf{k} \frac{\mathbf{k} \cdot \tilde{\mathbf{u}}(\mathbf{k})}{k^2} \mathbf{k} \exp\{2\pi i \mathbf{k} \cdot \ell\}, \quad (18)$$

is the inverse Fourier transform of the Fourier transformed velocity $\tilde{\mathbf{u}}(\mathbf{k})$ projected along the wave vector $\mathbf{k} = 2\pi/\ell$, where $\tilde{\mathbf{u}}(\mathbf{k})$ is defined,

$$\tilde{\mathbf{u}}(\mathbf{k}) = \frac{1}{N_{\text{grid}}^3} \int d\ell \mathbf{u}(\mathbf{x}) \exp\{-2\pi i \mathbf{k} \cdot \ell\}. \quad (19)$$

and Equation 17 is used to calculate \mathbf{u}_s . In Figure 4 we plot the mean normalized gas density, $\rho/\langle \rho \rangle_{\mathcal{V}}$ (top row), and the rms normalized magnitudes, $u_s/\langle u_s^2 \rangle_{\mathcal{V}}^{1/2}$ (middle row) and $u_c/\langle u_c^2 \rangle_{\mathcal{V}}^{1/2}$ (bottom row), components of velocity. In the left-hand column we show these fields at a time shortly after the beginning of the simulation, $t/t_0 = 4$, where the simulation is yet to form a time-stationary state (i.e., Equation 16). During this time it is straightforward to pick out the regions influenced by individual SNR, which are spheres of large density gradients around low-density interiors. It is also clear to see that the interiors of SNRs are closely associated with \mathbf{u}_s modes, while the SNe shock fronts are associated with \mathbf{u}_c modes. In the middle and right-hand column we show two-dimensional slices in the steady state (see Figure 3), $t/t_0 = 30$ and $t/t_0 = 37$, respectively. The density has collapsed in the $\nabla\phi$ direction, leading to a steeper gradient parallel to $\nabla\phi$, resulting in the disk being supported by both thermal, ∇P , and turbulent, ∇u^2 , pressure gradients. The effects of multiple, interacting SNRs become apparent for these t/t_0 , and turbulent velocity modes have developed over the entire simulation domain (see the middle row). Having gained a qualitative understanding of the velocity structures in our simulated ISM we now turn our attention to quantitative methods to dissect the energy spectrum and k space energy flux transfer, beginning with the velocity power spectrum.

Table 2. Velocity power spectrum parameters for MW_1024

	α_{\parallel}	α_{\perp}	$\ell_{\text{cor},\parallel}/\ell_0$	$\ell_{\text{cor},\perp}/\ell_0$
(1)	(2)	(3)	(4)	(5)
\mathbf{u}	1.63 ± 0.01	1.58 ± 0.03	4.1 ± 0.3	3.5 ± 0.3
\mathbf{u}_s	1.51 ± 0.02	1.51 ± 0.03	4.1 ± 0.3	3.3 ± 0.2
\mathbf{u}_c	2.08 ± 0.02	1.98 ± 0.02	4.5 ± 0.3	4.0 ± 0.3

Notes. Column (1): the velocity component, total, \mathbf{u} , incompressible, \mathbf{u}_s and compressible, \mathbf{u}_c . Column (2) and (3): the best fitting power law exponent to the power spectrum, $\mathcal{P}_u(k) \propto k^{-\alpha}$, along the parallel α_{\parallel} and perpendicular α_{\perp} directions to $\nabla\phi$. Column (4) and (5): the correlation length scale, Equation 24, along the parallel, $\ell_{\text{cor},\parallel}$, and perpendicular, $\ell_{\text{cor},\perp}$, directions in units of the gaseous scale height, ℓ_0 , where $\ell_0 \approx 85$ pc for $N_{\text{grid}} = 1,024$.

4. THE VELOCITY SPECTRA OF SUPERNOVA-DRIVEN TURBULENCE

We calculate the turbulent velocity power spectrum

$$\mathcal{P}_u(\mathbf{k}) = |\tilde{\mathbf{u}}(\mathbf{k})\tilde{\mathbf{u}}^{\dagger}(\mathbf{k})|, \quad (20)$$

where \dagger denotes the complex conjugate. Due to the acceleration from $\nabla\phi$, there is a global anisotropy in the

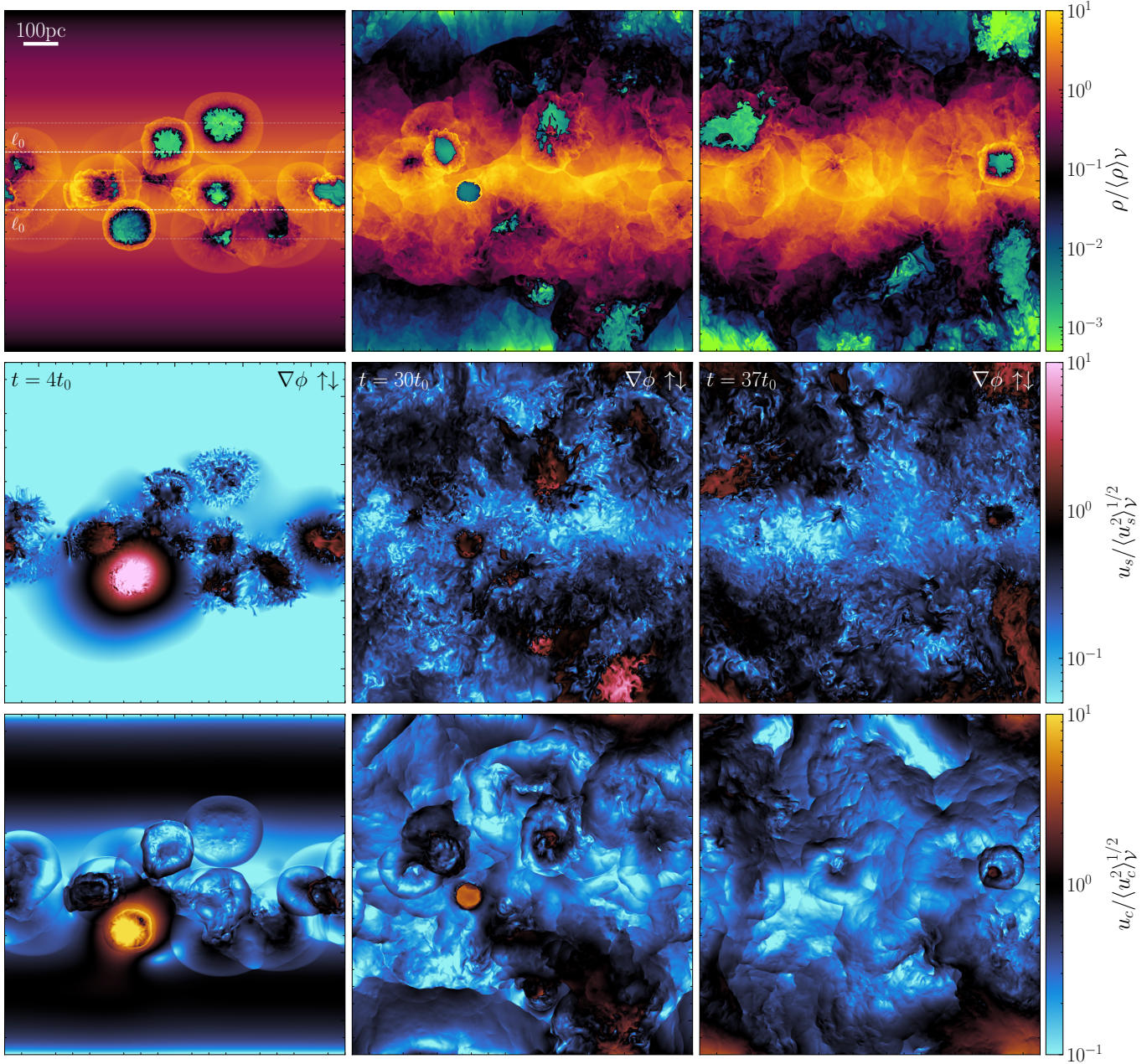


Figure 4. Two-dimensional slices parallel to $\nabla\phi$, through the center of the simulation domain, for the mass density, ρ (top row), incompressible (solenoidal) velocity, u_s ($\nabla \cdot \mathbf{u}_s = 0$; middle row) and compressible velocity, u_c ($|\nabla \times \mathbf{u}_c| = 0$; bottom row) at three different time realizations through the evolution of the simulation. All quantities are normalized by either the volume average in the case of the mass density $\langle \rho \rangle_V$, or the volume-weighted root-mean-squared (rms) for the velocities. The time of each snapshot is indicated in the panel on the middle row. The first snapshot is taken at the close to the beginning of the simulation $t \approx 4t_0$, the second just before the stationary state $t \approx 30t_0$ and the final in the stationary state, $t \approx 37t_0$ (see the full evolution of the turbulent Mach in Figure 3, which explicitly shows a steady state is reached within $t \sim 20t_0$). We show calculated gaseous scale height, ℓ_0 , with dashed white lines in the top left panel, as well as the midplane and $2\ell_0$ with more transparent white lines. Fluctuations in ρ and u_c are spatially correlated, with u_c generation corresponding to the expanding shock fronts ($\nabla \cdot \mathbf{u} < 0$) and the dilating regions inside of the remnants ($\nabla \cdot \mathbf{u} > 0$). Whilst u_s is more closely correlated with the post-shock regions and internal SNe structures, where the SNs generate intense regions of vorticity as they expand, eventually contributing to the vortical winds coming out of the disk.

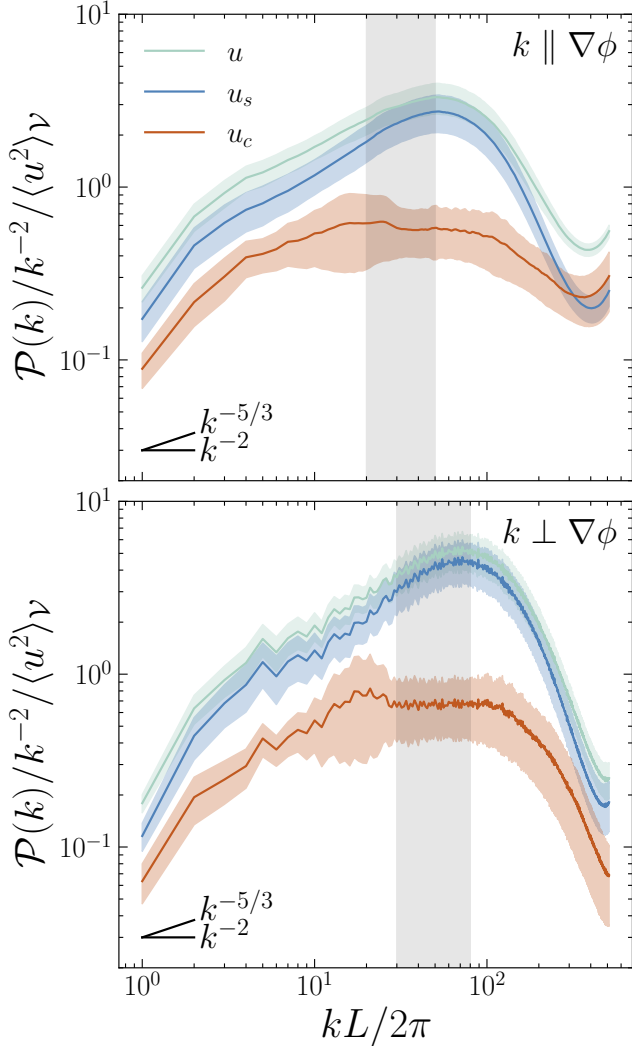


Figure 5. Cylindrically integrated, compensated velocity power spectra, $\mathcal{P}_u(k)$, as a function of wavenumbers parallel to the static gravitational potential $\nabla\phi$, Equation 8 ($k_{\parallel} = |k_z|$; top row) and perpendicular to it ($k_{\perp} = \sqrt{k_x^2 + k_y^2}$; bottom row). Each color represents either the total velocity \mathbf{u} (green), the incompressible velocity component of the velocity \mathbf{u}_s (blue) or the compressible component of the velocity \mathbf{u}_c (orange). All $\mathcal{P}_u(k)$ are compensated by the power in the total fluctuations $\langle u^2 \rangle_V$ (Equation 23), and k^{-2} for Burgers (1948)-type turbulence. The \mathbf{u}_s spectra approximately follow $\sim k^{-3/2}$ scaling and \mathbf{u}_c spectra a $\sim k^{-2}$ scaling, the Burgers (1948) expectation for Fourier transforms of velocity discontinuities (all exponents are reported in Table 2). A shaded gray region is shown where the inertial range, $\varepsilon = \text{const.}$, is very approximately true (see Appendix B).

velocity field which we must account for in the analysis of the spectra. Therefore we integrate the spectra into cylindrical wave numbers, which are defined as follows. Following the geometry of the galaxy disk we define two length scales, ℓ_{\parallel} and ℓ_{\perp} . The first, parallel to $\nabla\phi$, $\ell_{\parallel}^{-1} \sim$

$k_{\parallel} = |k_z|$, and the second, perpendicular to $\nabla\phi$ (parallel to the extent of the disk) $\ell_{\perp}^{-1} \sim k_{\perp} = \sqrt{k_x^2 + k_y^2}$. In our analysis we integrate the three-dimensional spectra into a two-dimensional function of these scales,

$$\mathcal{P}_u(k_{\parallel}, k_{\perp}) = \int d\Omega_{k_{\perp}} \mathcal{P}_u(\mathbf{k}) 2\pi k_{\perp}, \quad (21)$$

where $d\Omega_{k_{\perp}}$ is the angle-integration at fixed radial shells of k_{\perp} . We further integrate the $\mathcal{P}_u(k_{\parallel}, k_{\perp})$ along each dimension to achieve two one-dimensional spectra,

$$\mathcal{P}_u(k_j) = \int dk_i \mathcal{P}_u(k_i, k_j), \quad (22)$$

where all of our integrals conserve the total power in the field such that

$$\langle u^2 \rangle_V = \int dk \mathcal{P}_u(k), \quad (23)$$

i.e., Parseval's theorem. In Figure 5 we plot the integrated spectra of the total velocity \mathbf{u} and both the \mathbf{u}_s and \mathbf{u}_c components for the highest-resolution run (MW_1024). We normalize all spectra by $\langle u^2 \rangle_V$. The shaded regions around each spectrum denote the 1σ fluctuations from the time-average. For \mathbf{u} and \mathbf{u}_s the variation is generally quite small, while \mathbf{u}_c shows more substantial variation. As discussed in Section 3, \mathbf{u}_c is closely associated with SNe shock fronts and the large time variability in $\mathcal{P}_{u_c}(k)$ is likely tied directly to the stochastic nature of the SNe energy injections.

We identify a single inertial range for the spectra in each dimension, this is indicated by the shaded gray regions in each panel and is bracketed by $20 \lesssim k_{\parallel} \lesssim 50$ and $30 \lesssim k_{\perp} \lesssim 80$ for the parallel and perpendicular directions, respectively (see Appendix B for further discussion of the inertial range, but to summarize, we use the transfer functions from Section 5 to find where in k space is the $\varepsilon \approx \text{const.}$, i.e., the Kolmogorov definition). We calculate the correlation (outer) scale of turbulence along each dimension of the volume,

$$\frac{\ell_{\text{cor},i}}{L} = \frac{\int_0^{\infty} dk_i (kL/2\pi)^{-1} \mathcal{P}_u(k_i)}{\int_0^{\infty} dk_i \mathcal{P}_u(k_i)}. \quad (24)$$

In Table 2 we summarize ℓ_{cor} for all the velocity components. For \mathbf{u} we find $\ell_{\text{cor},\parallel} \approx 350 \text{ pc} \approx 4.1\ell_0$ and $\ell_{\text{cor},\perp} \approx 295 \text{ pc} \approx 3.5\ell_0$. Hence, in general, correlated turbulent motions exist on significantly larger scales than the gaseous scale height of the disk. The \mathbf{u}_s modes exhibit slightly shorter ℓ_{cor} than \mathbf{u}_c , albeit the differences are minor. The ℓ_{cor} s we list here are not significantly influenced by resolution – the values for the lower

resolution runs are included in Appendix E. Generally, $\ell_{\text{cor},\parallel} > \ell_{\text{cor},\perp}$ suggesting that the winds blowing out of the disk support correlated \mathbf{u} , \mathbf{u}_c and \mathbf{u}_s at larger physical scales than in $\ell_{\text{cor},\perp}$, larger than the classical \sim argument where the outer scale of the turbulence is set by the gaseous scale height (e.g., Beattie et al. 2022a). We return to this point in Section 5.3. In general, this means that we should consider the galactic winds and the ISM in the disk as being correlated, communicating through the turbulence, and that we should differentiate between driving scales ℓ_{inj} (≈ 2 pc for this simulation) and correlation scales, ℓ_{cor} (≈ 350 pc), i.e., a spectrum with energy peaked and correlated at low k does not mean the driving scale is also on low k , as inferred in Bialy & Burkhardt (2020); Colman et al. (2022).

Next, we fit a power law, $\mathcal{P}_u(k) \propto k^{-\alpha}$ to the spectra over the inertial range based on where the energy flux is approximately constant. The exact values with uncertainties are reported in Table 2. For the \mathbf{u} spectrum we find $\alpha_{\parallel} = 1.63 \pm 0.01$ and $\alpha_{\perp} = 1.58 \pm 0.03$, where the uncertainties are reported as 1σ errors on the fit. The \mathbf{u}_s spectrum is slightly shallower with indexes of $\alpha \approx 1.5$ in both directions, while the \mathbf{u}_c spectra are steeper showing $\alpha \approx 2$. The \mathbf{u}_c spectrum is consistent with Burgers (1948)-type turbulence with $\mathcal{P}_{u_c}(k) \sim k^{-2}$, whilst the \mathbf{u} spectrum is marginally consistent with Kolmogorov (1941)-type turbulence (which predicts a slope of $\alpha = 5/3 \approx 1.67$). Curiously, the \mathbf{u}_s spectrum deviates from Kolmogorov (1941), with a scaling close to the MHD Iroshnikov (1964)-Kraichnan (1965) spectrum $\alpha = 3/2$, with the shallower than Kolmogorov (1941) slopes found for magnetized supernova-driven turbulence Gent et al. (2021). However, as we highlight later in Section 5, the energy flux between the different \mathbf{u}_s modes can be mediated by \mathbf{u}_c , resulting in effects that strongly deviate from the classical Kolmogorov (1941) picture of turbulence (e.g., inverse cascades, negative energy fluxes). Our α values are broadly consistent with previous simulations of SNe detonations in a periodic box (Padoan et al. 2016), even though we have cylindrically integrated spectra and stratification.

It is noteworthy to further highlight that the α values that best fit each \mathbf{u} are quite similar to those found in Beattie et al. (2024). In the study, Beattie et al. (2024) modeled supersonic magnetohydrodynamic turbulence using Fourier space driving on large scales at extremely high resolution grids up to $10,080^3$. They also performed the decomposition of the $\mathcal{P}_u(k)$ into \mathbf{u}_c and \mathbf{u}_s modes, showing very similar spectral scalings as presented in this study (e.g., $\alpha \approx 3/2$ for incompressible and $\alpha \approx 2$ for compressible). The agreement between the values found here and those in Beattie et al. (2024) is sug-

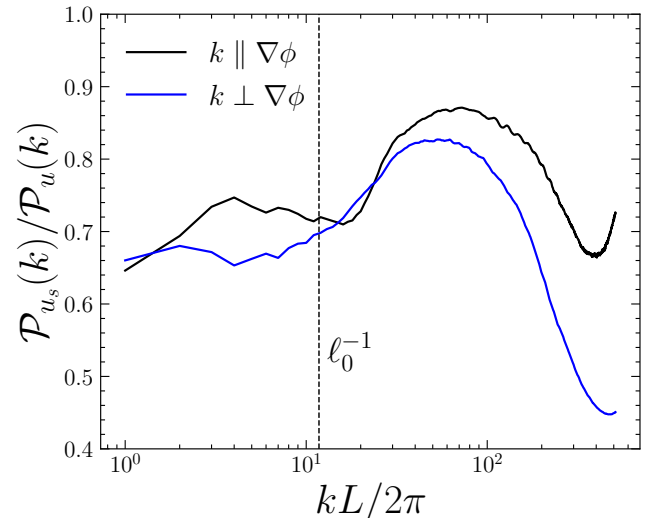


Figure 6. The ratio between the power spectrum of incompressible velocity modes $\mathcal{P}_{u_s}(k)$ and the total velocity modes $\mathcal{P}_u(k)$, $\mathcal{P}_{u_s}(k)/\mathcal{P}_u(k)$, colored by k_{\perp} (blue) and k_{\parallel} (black). The gaseous scale height ℓ_0 is indicated on the plot with the vertical black dashed line. The ratio shows that all scales in the ISM are dominated by \mathbf{u}_s modes, with a significant enhancement on scales $\ell \lesssim \ell_0$.

gestive that standard turbulent boxes, the workhorses of numerical turbulent experiments, may capture, to a certain degree, more realistic, global set-ups such as the one studied here, at least at the level of the spectrum, and at least for the compressible modes.

For all \mathbf{u} components, the slope of the spectra (and even the normalization) along each direction of $\nabla\phi$ is consistent with the same value to within $\sim 1\sigma$. This suggests that the SNe-driven turbulence in our simulation develops into fairly isotropic turbulence ($k_{\parallel} \sim k_{\perp} \sim |\mathbf{k}|$) on small enough ℓ (or high enough k), despite the presence of the stratification from $\nabla\phi^1$. Such universality is regularly invoked for turbulence at the small scales (e.g., Nazarenko & Schekochihin 2011) and has previously been realized for a number of different global ge-

¹ Given the nature of the geometry of the disk splitting scales into parallel ℓ_{\parallel} and perpendicular ℓ_{\perp} along the $\nabla\phi$, stratified turbulence theory (e.g., Maffioli 2017) is a natural framework to consider for explaining the measured spectra. However, our simulations, and potentially in general supernova-driven turbulence, fail to meet the basic assumptions that the stratified models have. Specifically, the components of the velocity field modeled here are very similar along and across $\nabla\phi$, $u_{\parallel} \sim u_{\perp}$, whereas stratified turbulence theory assumes $u_{\parallel} \ll u_{\perp}$. Hence, even though we have a disk structure the turbulence is rather isotropic and is not strongly stratified. Regardless, we retain the ℓ_{\parallel} and ℓ_{\perp} decomposition of the domain demanded upon us by $\nabla\phi$, which will certainly be an appropriate framework for understanding longer box setups, where the stratification will play a more significant role, as in, e.g., Kim & Ostriker (2017).

ometries (Schumacher et al. 2014). This is potentially part of the reason why the spectral exponents end up being quite similar to the local models.

Interesting to understand is the ratio between the power in the \mathbf{u}_s and \mathbf{u}_c modes as a function of k , which allows us to understand what kinds of modes dominate each scale in the ISM (Federrath et al. 2010; Padoan et al. 2016; Pan et al. 2016; Li et al. 2020). We plot $\mathcal{P}_{u_s}(k)/\mathcal{P}_u(k)$ in Figure 6, for both of the two directions, indicated with the color. The turbulence is dominated by incompressible modes $\mathcal{P}_{u_s}(k)/\mathcal{P}_u(k) \gtrsim 0.6$, which usually is the case, and has been found before for supernova-driven turbulence (Padoan et al. 2016; Pan et al. 2016; Gent et al. 2021), and even for turbulent boxes driven with purely compressible modes (top right panel Figure 8 in Federrath 2013). On $k > \ell_0^{-1}$, i.e., smaller ℓ than the gaseous scale height, the \mathbf{u}_s modes become highly energized, even more so than in purely incompressible-driven turbulent boxes (top left panel Figure 8 in Federrath 2013). We will address the most likely candidate for the intense surge of incompressible mode power in Section 6. Regardless of the source, the key result from Figure 6 is that even in the presence of purely compressible driving, the velocity modes are dominated by the \mathbf{u}_s component, even more so in supernova-driven turbulence than in turbulent boxes.

The $\mathcal{P}_u(k)$ provides some first-order understanding of the nature of SNe-driven turbulence in the ISM (e.g., Fourier amplitudes of the velocity \iff the distribution of the second moment of velocity across k space, which one can directly model), but the spectrum alone is insufficient to differentiate between different types of turbulence. Motivated strongly by the work of Grete et al. (2017a), to gain a deeper understanding of the type of turbulence energy interactions, we turn our attention to the spectral energy transfer functions.

5. SPECTRAL TRANSFER FUNCTIONS

With the goal of understanding the underlying turbulent cascade mechanisms and nature of the energy flux, we utilize shell-to-shell energy transfer functions based on Grete et al. (2017a), and for an incompressible plasma, see Alexakis et al. 2005). This method allows us to both probe ε between sets of k -mode shells, K and Q , and associate it with a particular mechanism directly from the momentum equation of the fluid, Equation 4. Because we are also interested in interactions between \mathbf{u}_c and \mathbf{u}_s , and how they might differ, we take the Grete et al. (2017a) method a step further and decompose the transfers into incompressible and compressible mode interactions, which we detail in the following subsection.

5.1. Helmholtz-decomposed transfer functions

The turbulent cascade arises from the quadratic nonlinearity in Equation 4, $\mathbf{u} \cdot \nabla \otimes \mathbf{u}$ (Kraichnan 1971; Waleffe 1992; Alexakis et al. 2005), therefore, to keep this analysis as simple as possible, we focus solely on this $\mathbf{u} \cdot \nabla \otimes \mathbf{u}$ for the kinetic energy transfer functions, where the nonlinearity becomes $\mathbf{u} \cdot \mathbf{u} \cdot \nabla \otimes \mathbf{u} = \mathbf{u} \otimes \mathbf{u} : \nabla \otimes \mathbf{u} = u_i u_j \partial_j u_i$,² which can be filtered to construct the transfer function,

$$\mathcal{T}_{uu}^u(Q, K|P) = - \int d^3\ell \mathbf{u}^K \otimes \mathbf{u}^P : \nabla \otimes \mathbf{u}^Q, \quad (25)$$

to indicate the transfer of energy flux from shell Q to K , mediated by \mathbf{u}^P , where, e.g., $\mathbf{u}^K(\ell)$ is the real space value of \mathbf{u} integrated over the cylindrical integrated k -mode shell K (see Section 5.2 for more details on the shell definitions). In general, the transfer function probes the interaction between three velocity modes, $\mathbf{k}^Q + \mathbf{k}^P + \mathbf{k}^K = 0$. However, following Mininni et al. (2005) and Grete et al. (2017a), we do not require knowing the localization of the \mathbf{u}^P mode, and hence we sum over all mediating P mode shells (simply giving the total velocity), which is therefore

$$\mathcal{T}_{uu}^u(Q, K) = - \int d^3\ell \mathbf{u}^K \otimes \mathbf{u} : \nabla \otimes \mathbf{u}^Q. \quad (26)$$

This means that our transfer functions are not able to localize the interaction (mediated by \mathbf{u}^P), but can localize the transfer of energy flux from \mathbf{u}^Q to \mathbf{u}^K (Mininni et al. 2005; Alexakis et al. 2005; Grete et al. 2017b).

In this study, we are interested in the interplay between the compressible and incompressible modes, which we can separate in the velocity via the Helmholtz decomposition as in Equation 17. By applying it to Equation 26, we get

$$\begin{aligned} \mathcal{T}_{uu}^{c+s}(Q, K) = & \quad (27) \\ & - \int d^3\ell (\mathbf{u}_c^K + \mathbf{u}_s^K) \otimes (\mathbf{u}_c + \mathbf{u}_s) : \nabla \otimes (\mathbf{u}_c^Q + \mathbf{u}_s^Q), \end{aligned}$$

hence we can calculate transfers between \mathbf{u}_c and \mathbf{u}_s , mediated by either $\mathbf{u}_s \cdot \nabla$ or $\mathbf{u}_c \cdot \nabla$. We can write

² Note that this can be directly related to Equation 1 through the triple product $\partial_i(u_i u_j u_j) = u_j u_j \partial_i u_i + 2u_i u_j \partial_i u_j$ using the symmetry of the $u_i u_j$ tensor. For incompressible turbulence $\partial_i(u_i u_j u_j) = 2u_i u_j \partial_i u_j$, so the exact relations we report in Section 1 are proportional to the incompressible transfer functions that we derive in this section, as expected.

transfer functions between like-modes as follows,

$$\mathcal{T}_{cc}^c(Q, K) = - \int d^3\ell \mathbf{u}_c^Q \xrightarrow{\mathbf{u}_c} \mathbf{u}_c^K \otimes \mathbf{u}_c : \nabla \otimes \mathbf{u}_c^Q, \quad (28)$$

$$\mathcal{T}_{cc}^s(Q, K) = - \int d^3\ell \mathbf{u}_c^Q \xrightarrow{\mathbf{u}_s} \mathbf{u}_c^K \otimes \mathbf{u}_s : \nabla \otimes \mathbf{u}_c^Q, \quad (29)$$

$$\mathcal{T}_{ss}^c(Q, K) = - \int d^3\ell \mathbf{u}_s^Q \xrightarrow{\mathbf{u}_c} \mathbf{u}_s^K \otimes \mathbf{u}_c : \nabla \otimes \mathbf{u}_s^Q, \quad (30)$$

$$\mathcal{T}_{ss}^s(Q, K) = - \int d^3\ell \mathbf{u}_s^Q \xrightarrow{\mathbf{u}_s} \mathbf{u}_s^K \otimes \mathbf{u}_s : \nabla \otimes \mathbf{u}_s^Q, \quad (31)$$

where we provide both the full transfer function definition and shorthand notation, e.g., $\mathbf{u}_a \xrightarrow{\mathbf{u}_b} \mathbf{u}_c$, to emphasize that the notation $\mathcal{T}_{ab}^c(Q, K)$ means a -type modes in shell Q donate ($\mathcal{T} > 0$) energy to b -type modes in shell K via mediation by any c -type modes. For example, the $\mathcal{T}_{ss}^c(Q, K)$ transfer function (or concisely written, $\mathbf{u}_s \xrightarrow{\mathbf{u}_c} \mathbf{u}_s$) describes the local energy flux from incompressible \mathbf{u}_s modes in shell Q to incompressible \mathbf{u}_s modes in shell K , mediated by a compressible mode interaction $\mathbf{u}_c \cdot \nabla$ from an unspecified shell. We will regularly use the $\mathbf{u}_a \xrightarrow{\mathbf{u}_b} \mathbf{u}_c$ and \mathcal{T}_{ab}^c notation throughout the rest of the study. With these transfer functions, we can probe not only the location, extent, and directionality of the turbulent cascade in our SNe-driven turbulence simulations, but also the nature of \mathbf{u}_c and \mathbf{u}_s mode interactions.

An important property of any transfer function is antisymmetry, i.e., $\mathcal{T}(Q, K) = -\mathcal{T}(K, Q)$ (Mininni et al. 2005; Alexakis et al. 2005; Grete et al. 2017b). We address the preservation of the antisymmetry property for the $\mathcal{T}(Q, K)$ in Appendix C, highlighting three important aspects. The first is that there is a violation in the antisymmetry with the outflow boundary conditions in our simulation, as expected. We show later that this ends up being quite negligible. However, important for our unique Helmholtz decomposed transfer functions is that the antisymmetric property for \mathbf{u}_s and \mathbf{u}_c mediated $\mathcal{T}(Q, K)$ are different. Indeed, we show that \mathbf{u}_s mediated transfers are antisymmetric with themselves, but \mathbf{u}_c mediated transfers are not, and require an additional transfer mediated by $\nabla \cdot \mathbf{u}_c$ (see Equation C10 for more details).

There also exists a set of transfer functions for flux transfers between mixed modes ($\mathbf{u}_s \xrightarrow{\mathbf{u}_c, \mathbf{u}_s} \mathbf{u}_c$ and

$\mathbf{u}_c \xrightarrow{\mathbf{u}_c, \mathbf{u}_s} \mathbf{u}_s$), these interactions carry less energy flux and therefore we limit our analysis in the main text to just the like-mode transfers. However, the energy flux between mixed modes transfers is still generally interesting because it describes the process of turning \mathbf{u}_c modes from detonating SNe directly into \mathbf{u}_s modes, which define the classical turbulence cascade; for this reason, we include the mixed-mode transfers and the discussion of them in Appendix A.

5.2. Shell definition

We define our shells in the cylindrical coordinate system (see Section 4). For perpendicular scales, $\ell \perp \nabla\phi$, it is

$$\mathbf{u}_\perp^K(\ell) = \int d\mathbf{k} \delta^2(k_\perp - K) \tilde{\mathbf{u}}(\mathbf{k}) \exp\{2\pi i \mathbf{k} \cdot \ell\}, \quad (32)$$

and for parallel scales it is,

$$\mathbf{u}_\parallel^K(\ell) = \int d\mathbf{k} \delta(|k_\parallel| - K) \tilde{\mathbf{u}}(\mathbf{k}) \exp\{2\pi i \mathbf{k} \cdot \ell\}, \quad (33)$$

without loss of generality. In the Equation 32 $\delta^2(k_\perp - K)$ is the two-dimensional delta function that selects the K shell from the cylindrical k_\perp coordinate, and the same for $\delta(|k_\parallel| - K)$ but for the one-dimensional delta function, since the k_\parallel is one-dimensional. Each set of K and Q shells are chosen to be logarithmically spaced, such that the shell edges are given by,

$$\{Q_i\} = \{K_i\} = \left\{2^{(i-1)/4+2}\right\}, \quad (34)$$

$$i = 0, \dots, 4 \frac{\ln(N_{\text{grid}}/8)}{\ln(2)} + 1, \quad (35)$$

where N_{grid} is the number of resolution elements per linear dimension (i.e., $N_{\text{grid}} = 1024$ for the 1024^3 simulation). This allows us to extract turbulent eddies that are local in log space, rather than specific wave modes, which are local in linear space, as discussed in Grete et al. (2017b). Because we compute the transfer functions for both ℓ_\parallel and ℓ_\perp , we have a total of 20 transfer functions, considering all of the $\mathbf{u} \rightarrow \mathbf{u}$, $\mathbf{u}_c \rightarrow \mathbf{u}_c$, $\mathbf{u}_s \rightarrow \mathbf{u}_s$ and $\mathbf{u}_c \leftrightarrow \mathbf{u}_s$ energy flux transfers.

5.3. Shell-to-shell energy transfer

In Figure 7 we visualize the shell-to-shell energy transfer between velocity like-modes ($\mathbf{u}_c \rightarrow \mathbf{u}_c$ or $\mathbf{u}_s \rightarrow \mathbf{u}_s$ fluxes). The top row of the figure contains the transfers in k_\parallel , whilst the bottom row includes the transfers in k_\perp . Each column contains a particular three mode transfer type, which is indicated in the top left hand corner of the panel. As with the spectrum in Section 4, there is not a large difference between k_\parallel and k_\perp , so we

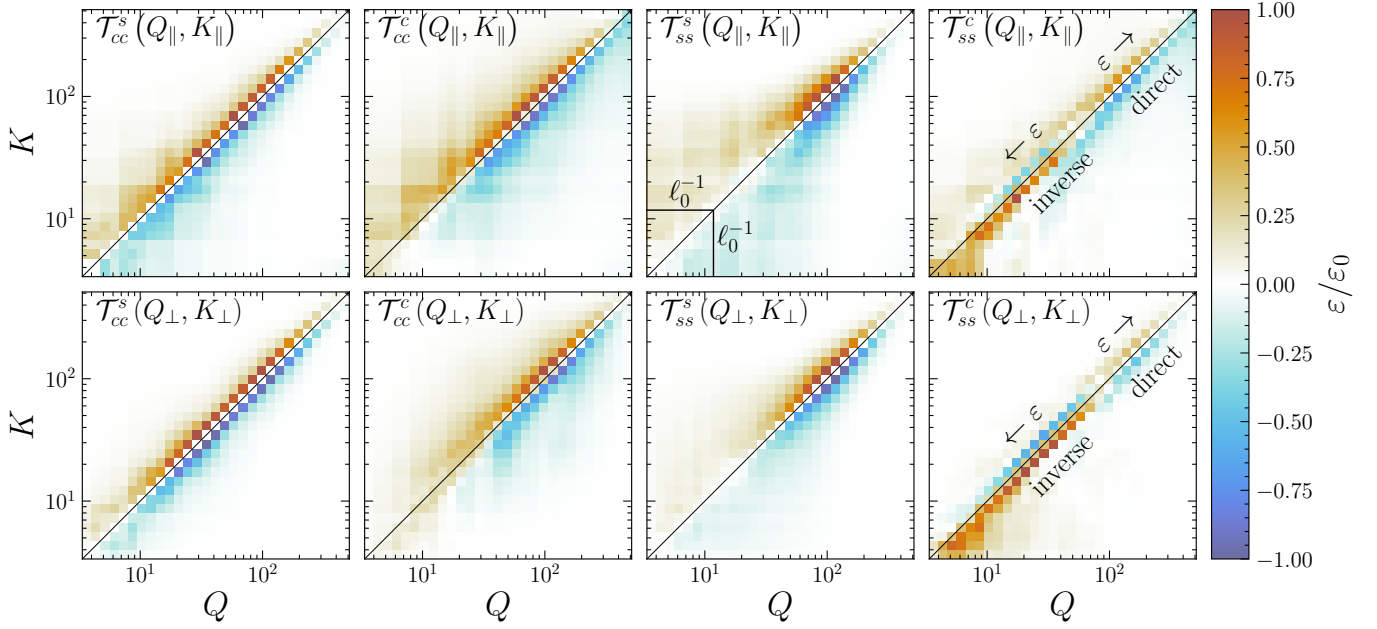


Figure 7. Time averaged shell-to-shell transfer of kinetic energy between logarithmic shells, with transfers parallel to the gravitational potential (k_{\parallel} ; top row) and perpendicular to it (k_{\perp} ; bottom row). All transfers are between like-modes ($\mathbf{u}_c \leftrightarrow \mathbf{u}_c$ or $\mathbf{u}_s \leftrightarrow \mathbf{u}_s$) of velocity, Equation 28–Equation 31, colored by the energy flux ε , normalized to the maximum, absolute value, ε_0 , in each transfer. The black horizontal and vertical lines in the $\mathcal{T}_{ss}^s(Q_{\parallel}, K_{\parallel})$ panel indicate k of the disk scale height, $k_0 \sim \ell_0^{-1}$ (Section 2.1.2). Most compressible \mathbf{u}_c and incompressible \mathbf{u}_s modes exhibit direct turbulent cascades (positive energy flux from large to small scales). However, $\mathbf{u}_s \rightarrow \mathbf{u}_s$ mediated by \mathbf{u}_c interactions exhibits an inverse (negative energy flux) cascade at small to large scales. This takes energy from below the disk scales $k > k_0$, out to larger scales, $k < k_0$, potentially then fueling the direct cascades in the other transfer functions (and e.g., the winds out of the disk). Shell-to-shell transfers between mixed-modes are included in Appendix A.

will discuss the trends found for the flux transfer across both the directions at the same time. When expanding out each transfer function in terms of its triple product one finds a surface flux term, $\sim \oint_{\partial\mathcal{V}} u_i u_j u_i d\mathcal{V}_j$ that disappears in the triply-periodic case. This does not strictly disappear for our simulations, but one can probe how large the effect is by looking for deviations away from $\mathcal{T}(Q, K) = -\mathcal{T}(K, Q)$ in the \mathbf{u}_s mediated transfers (see Appendix C). In Figure 7 we see perfect antisymmetry in all \mathbf{u}_s mediated transfers, hence we conclude $\oint_{\partial\mathcal{V}} u_i u_j u_i d\mathcal{V}_j \approx 0$, preserving the $\mathcal{T}(Q, K) = -\mathcal{T}(K, Q)$ property.

5.3.1. Compressible to compressible mode energy flux

We begin with the energy flux $\mathbf{u}_c \rightarrow \mathbf{u}_c$, corresponding to either \mathcal{T}_{cc}^c or \mathcal{T}_{cc}^s (1st column in Figure 7). Both of these transfers exhibit direct energy cascades from large to small scales, regardless of the mediating mode or the direction. \mathcal{T}_{cc}^s supports a highly localized direct cascade which extends over most of the k -modes in both k_{\parallel} and k_{\perp} . This may potentially be from the post-shock regions (energetically dominated by \mathbf{u}_s ; see Figure 13 in Hew & Federrath 2023) scattering \mathbf{u}_c modes down a cascade. This is quite peculiar since the \mathbf{u}_c power spectrum

is $u_c^2(k) \sim k^{-2}$ (see Figure 5), which is usually interpreted as Burgers (1948). But Burgers (1948) is highly non-local, in that k^{-2} comes from Fourier transforming a single velocity discontinuity (a single real-space structure transforms to all k -modes). Clearly this is not what is happening in the \mathcal{T}_{cc}^c transfers, which has the most extended and local cascade out of all of the transfers functions. Based on this result, we can confidently say that there is a \mathbf{u}_c mode cascade, but it is mediated by interacting with \mathbf{u}_s modes.

Now we turn our focus to the three-mode interaction \mathcal{T}_{cc}^c (2nd column in Figure 7). This transfer function shows a direct cascade over a large range of k modes that is much less localized than \mathcal{T}_{cc}^s (much more energy flux in the off-diagonal components). This is potentially associated with Burgers (1948)-type of turbulence (i.e., not a cascade, just non-local dumping of energy), indicating that the energy flux imprint from the velocity discontinuities is contained within the \mathcal{T}_{cc}^c transfer but not within \mathcal{T}_{cc}^s . The source of mediating \mathbf{u}_c modes in the \mathcal{T}_{cc}^c transfers is of course the SNe detonations, hence we may consider \mathcal{T}_{cc}^c as a probe of the energy flux from the interactions of the expanding shells with the $\mathbf{u}_c \rightarrow \mathbf{u}_c$ cascade, somewhat visualized in the bottom row of Fig-

ure 4. Since both the \mathcal{T}_{cc}^c and \mathcal{T}_{cc}^s mode interactions transfer energy flux between $\mathbf{u}_c \rightarrow \mathbf{u}_c$ modes, both of these interactions contribute to the spectrum in $u_c^2(k)$, shown in Figure 5. Based on the total energy fluxes in and out of each Q and K (the coss scale transfer) in Appendix B, the \mathcal{T}_{cc}^c energy flux is significantly larger than \mathcal{T}_{cc}^s , so \mathcal{T}_{cc}^c is a much faster³ cascade (energy moves faster to high k with \mathcal{T}_{cc}^c). Regardless of the absolute values of the flux, what we have shown here by separating out \mathcal{T}_{cc}^s from \mathcal{T}_{cc}^c , is that even though the $u_c^2(k) \sim k^{-2}$ spectrum is regularly associated with the Burgers (1948)-type phenomenology (e.g., Federrath 2013), there is a real $\mathbf{u}_c \rightarrow \mathbf{u}_c$ cascade component of this transfer that is highly local in \mathbf{u}_c , when mediated by \mathbf{u}_s .

5.3.2. Incompressible to incompressible mode energy flux

Now to the incompressible $\mathbf{u}_s \rightarrow \mathbf{u}_s$ transfers, i.e., \mathcal{T}_{ss}^s and \mathcal{T}_{ss}^c (3rd column in Figure 7). The \mathcal{T}_{ss}^s transfers are the classical Kolmogorov-type transfer, where Equation 1 should hold. Interestingly, these transfers are the most non-local out of all of the energy fluxes, with all $kL/2\pi \lesssim 50$ (well above to below the gaseous scale height) being dominated by non-local low energy flux transfers across the modes. It is only when we get to $k \gtrsim 30$ modes, i.e., $\ell \lesssim 30$ pc, where we see something that starts to resemble a more local cascade, but these scales have a significant numerical viscous component, as discussed in Section 2.2. This is interesting because, as we showed in Figure 5, the $u_s^2(k) \sim k^{-3/2}$ spectrum is self-similar over a large range of scales (e.g., $4 \lesssim k_\perp \lesssim 80$ and same for k_\parallel), which includes most of the scales here that are dominated by non-local transfers. Indeed, this would suggest that the self-similar region of the spectrum is not at all generated from local transfers, á la Kolmogorov. In fact, it seems like the compressible modes, in general, are undergoing much more local cascades, which is completely at odds with the conventional wisdom for supersonic turbulence.

Strikingly, the \mathcal{T}_{ss}^c (4th column in Figure 7) supports both an inverse and a direct cascade, where the flux for the inverse cascade is significantly stronger than the forward one (energy is transported more efficiently up, i.e., $\varepsilon < 0$, than down, i.e., $\varepsilon > 0$). The inverse cascade extends over a significant range of k modes, extending well beyond ℓ_0^{-1} , and into the galactic winds. Like \mathcal{T}_{ss}^s , a small region of net zero ε exists between the inverse and the direct cascades, although this region is much more

localized than is seen for \mathcal{T}_{ss}^s . In Section 5.4 we examine more closely the mechanisms for establishing and supporting the inverse transfer of energy, but already we can assume that this is not a standard incompressible inverse cascade, which is mediated by helical \mathbf{u}_s modes (Plunian et al. 2020). Indeed, this is one of the key results in this paper – the compressible mode mediated $\mathbf{u}_c \rightarrow \mathbf{u}_c$ transfer functions support a direct $\varepsilon > 0$ and inverse $\varepsilon < 0$ cascade. In both the ℓ_\parallel and ℓ_\perp directions in \mathcal{T}_{ss}^c there is also significant energy loss at $k \lesssim k_0$ (red lobes in \mathcal{T}_{ss}^c at low k , which indicate energy coming out of those modes). This is potentially evidence for feeding the other cascade with the inverse fluxes. We explore this in a little more detail in Appendix A.

Let us summarize these last two paragraphs, because this is a point that needs to be emphasized. In the self-similar range of the incompressible power spectrum ($\mathcal{P}_{u_s}(k) \sim k^{-\alpha}$; shown in Figure 5), the energy flux transfers are direct but strongly non-local when we consider $\mathbf{u}_s \xrightarrow{u_s} \mathbf{u}_s$ transfers, and inverse but local when we consider $\mathbf{u}_s \xrightarrow{u_c} \mathbf{u}_s$ transfers. These are the two types of transfers that make up the incompressible mode cascade. This is completely unlike the Kolmogorov (1941) phenomenology for hydrodynamical turbulence, which is local and direct. Because the \mathbf{u}_s cascade is energetically dominant, and because it is a mixture of $\varepsilon > 0$ and $\varepsilon < 0$, this will act to reduce the total ε , potentially softening the cascade and creating deviations from the strongly nonlinear, local Kolmogorov (1941) case, which we showed is evident in $\mathcal{P}_{u_s}(k)$ in Section 4. Finally, these energy flux results do not resemble local box turbulence simulations from Grete et al. (2017a), where there is no evidence for inverse cascades and where the \mathbf{u}_c mediated transfers were shown to be more non-local than the classical advective ones. However, note that Grete et al. (2017a) did not perform the Helmholtz decomposed transfers, so indeed, the energy fluxes we probe here are different, e.g., Grete et al. (2017a) investigated $\sim u_i^Q u_i^K \partial_j u_{j,c}$ and we investigate $u_i^Q u_{j,c} \partial_j u_i^K$ (we show the relation between these transfer functions in Equation C10).

5.4. Unraveling the inverse cascade mechanism

Now we intend to provide direct evidence for the mechanism responsible for driving the inverse cascade seen in the rightmost panels of Figure 7. In Figure 8 we show two-dimensional slices of the $\mathcal{T}_{ss}^c(Q_\perp, K_\perp)$ transfer function before we integrate it, i.e., the spatial slices of

$$\mathcal{T}_{ss}^c(x, y, z) = -\mathbf{u}_s^{K_\perp} \otimes \mathbf{u}_c : \nabla \otimes \mathbf{u}_s^{Q_\perp}, \quad (36)$$

from a single time realization of the simulation, normalized by the mean energy flux ε_0 , and filtered at

³ We say “faster” in that ε and the cascade rate, t_{nl}^{-1} are related by $\varepsilon \propto t_{nl}^{-3}$ (assuming Kolmogorov turbulence, $u \sim (\varepsilon \ell)^{1/3}$, and $t_{nl}^{-1} \sim u/\ell$), hence larger ε means a faster cascade, which intuitively makes sense.

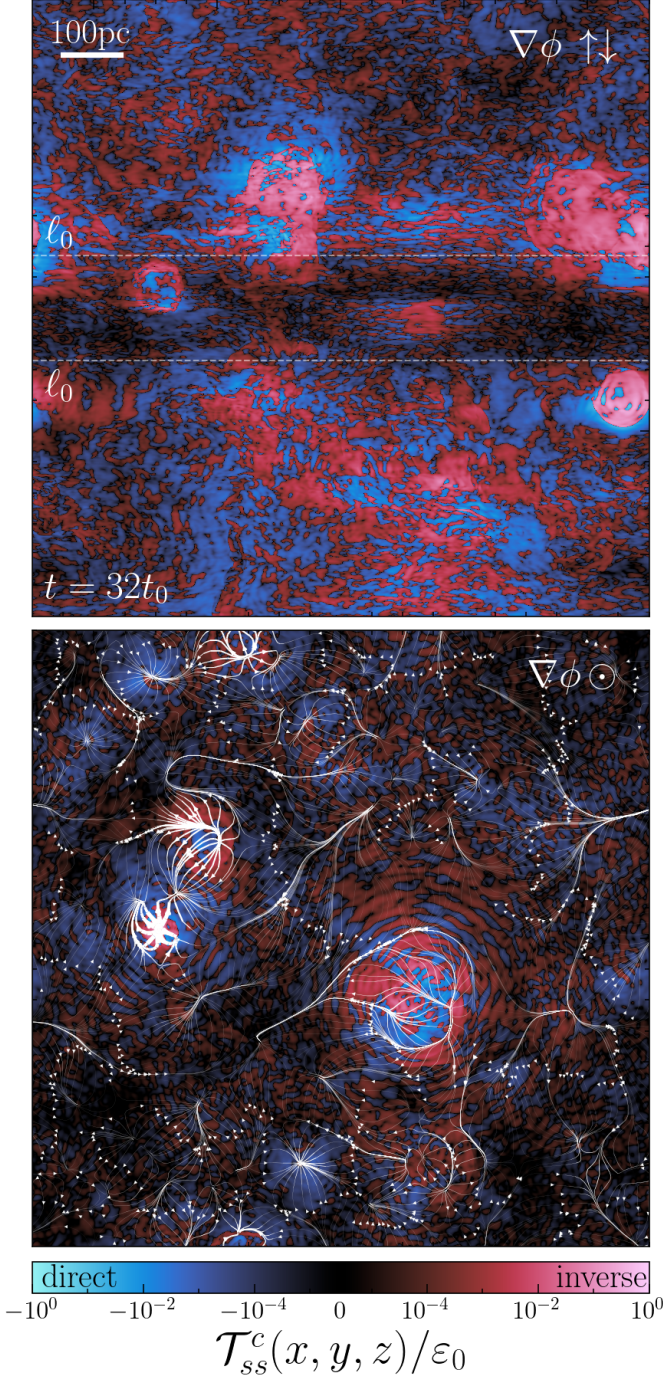


Figure 8. Two-dimensional slices of $\mathcal{T}_{ss}^c(x, y, z)$ (the energy flux between \mathbf{u}_s modes mediated by \mathbf{u}_c modes; Equation 36), Fourier filtered over $11 \leq k_\perp \leq 45$ with $Q_\perp < K_\perp$, covering the range of modes where the inverse cascade is observed in the \mathcal{T}_{ss}^c transfer function (see bottom right hand panel of Figure 7). For $\mathcal{T}_{ss}^c > 0$ (red) the region of space is undergoing an inverse cascade, and for $\mathcal{T}_{ss}^c < 0$ (blue), a direct cascade. In the top panel the slice is parallel to $\nabla\phi$ through the center of the domain, with the measured gaseous scale height ℓ_0 annotated in a similar way as in Figure 4. In the bottom panel we slice perpendicular to $\nabla\phi$, through the center of the galactic disk.

$11 \leq k_\perp \leq 45$ with $Q_\perp < K_\perp$, to ensure that we pick the structures inside of the inverse cascade that we showed in Figure 7. The top panel shows the energy transfer in a $\parallel \nabla\phi$ slice, and the bottom panel shows a $\perp \nabla\phi$ slice. $\mathcal{T}_{ss}^c(x, y, z) > 0$ (red) corresponds to regions that participate in the inverse cascade, whilst $\mathcal{T}_{ss}^c(x, y, z) < 0$ (blue) corresponds to the regions participating in the direct cascade, as indicated in annotations on the colormap. We filter and add a slice of the \mathbf{u}_c vector field streamlines to the bottom panel, with the streamlines weighted by $|\nabla \cdot \mathbf{u}_c|$ to expose the correlation between $\mathcal{T}_{ss}^c(x, y, z)$ and the convergence $\nabla \cdot \mathbf{u} < 0$ and $\nabla \cdot \mathbf{u} > 0$ divergence of \mathbf{u}_c . This might be the first plot that directly visualizes the direction of a turbulent cascade as a function of space.

Immediately, one can observe a plethora of detailed fluctuations in $\mathcal{T}_{ss}^c(x, y, z)$. From the top panel, we see the winds coming out of the disk have regions with significant $\mathcal{T}_{ss}^c(x, y, z) > 0$, where the inverse cascade is the strongest. Indeed, in most places in the winds we see inverse cascade, indicating that the \mathbf{u}_c modes contribute to energizing low- k vortical modes in the galactic winds. Active SNe detonations are also bright red, indicating that the inverse cascade is strongly correlated with SNe detonation events. This is also demonstrated in the bottom panel, where the \mathbf{u}_c modes are mostly diverging out of red regions and mostly converging into blue regions.

As we suggested in Section 5, this demonstrates that the \mathbf{u}_c modes from SNe detonations drive \mathbf{u}_s modes to lower k modes, by advecting, $\mathbf{u}_c \cdot \nabla$, and stretching, $\nabla \otimes \mathbf{u}_s^{Q_\perp}$, them around the SNe shells. This is qualitatively similar to the FRB model proposed by Thompson (2023), where Alfvén modes are stretched by an expanding outflow around a magnetar (see Thompson’s figure 2). Note that this is not a $u_i^K u_i^Q \partial_k u_k^P$ transfer of energy flux where the compressible mode is mediating the transfer via divergence. It is an advective process, where \mathbf{u}_s modes move to lower k modes by interacting (or scattering) with $\mathbf{u}_c \cdot \nabla$, i.e., this is really an inverse cascade and not simply an expansion, which would be probed by a $u_i^K u_i^Q \partial_k u_k^P$ type transfer function. This is a completely new mechanism for inverse cascade, that does not have anything obviously associated with the helicity of the \mathbf{u}_s modes, as required in inverse cascades in three-dimensional incompressible turbulence (Plunian et al. 2020, see Section 5.4 for further details about the global helicity in these simulations), but a more detailed analysis of the local helicity of the \mathbf{u}_s modes is required to discuss the detailed deviations.

We close this subsection with an interesting observation that the $\mathbf{u}_s \xrightarrow{\mathbf{u}_c} \mathbf{u}_s$ transfers are rather suppressed

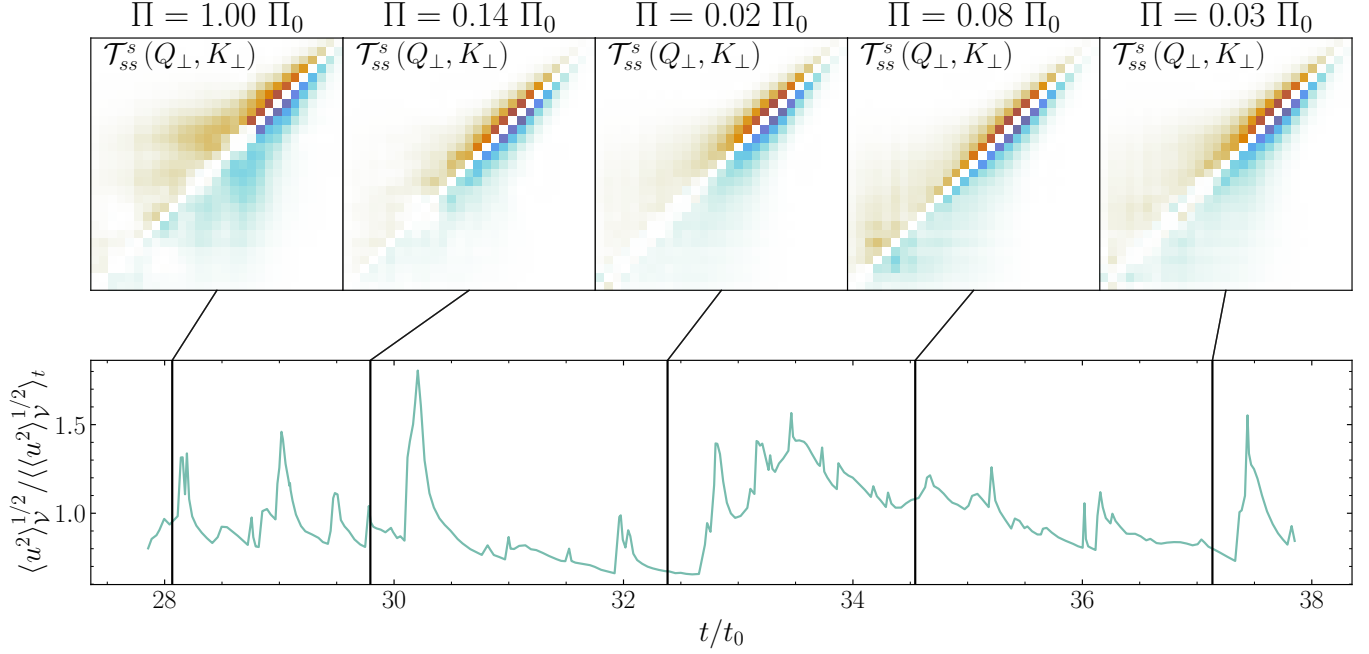


Figure 9. Top: The shell-to-shell energy transfers $\mathbf{u}_s \rightarrow \mathbf{u}_s$ modes, mediated by \mathbf{u}_s modes, \mathcal{T}_{ss}^s (Equation 31; i.e., the transfer function that would capture the classical, incompressible, Kolmogorov (1941)-type cascade), for the five time realizations averaged over in the transfer function analysis. The extent (how many k modes in the cascade), direction of cascade (whether it is inverse or direct) and the total energy flux Π/Π_0 , changes significantly between different realizations in the stationary state, indicating that the entire ISM cascade fluctuates significantly in time. **Bottom:** The time evolution of $\langle u^2 \rangle_{\mathcal{V}}$, normalized by the time-averaged $\langle u^2 \rangle_{\mathcal{V}}$, within the stationary state of the simulation.

within the disk, which is best visualized in the top panel of Figure 8, where we have added $|\ell_0|$ contours. This just means that the $\mathbf{u}_s \xrightarrow{u_c} \mathbf{u}_s$ transfer is rather low-volume filling factor in the galactic disk, mostly concentrated close to SNRs and in the galactic winds. An interesting future endeavor would be to use the diagnostics we have developed in this section to understand how inhomogeneous other types of energy fluxes are, e.g., those in Grete et al. (2017a) throughout a galaxy (one can imagine extending our preliminary analysis by computing poloidal, toroidal and radial ε profiles for many different types of energy flux). Of course, this will not only result in a better understanding of how turbulence works in our own Galaxy, but be critical for understanding how heating and cooling work in turbulent plasmas, which are directly related to the energy flux (e.g., Howes 2024; Mohapatra & Quataert 2024).

5.5. Time variability of the Kolmogorov cascade

As observed in Section 2.2 (specifically, the strong time variability in Figure 3), our ISM is subject to considerable time variability, at least in $\langle u^2 \rangle_{\mathcal{V}}^{1/2}$ (the square root total energy in the fluctuations integrated over $\mathcal{P}_u(k)$; Equation 23). Hence, before concluding this section we examine the nature of the variability in $\mathcal{T}(Q, K)$, which should translate to variability in both

slope and extent of the cascade. Figure 9 shows the $\mathcal{T}_{ss}^s(Q_{\perp}, K_{\perp})$ shell-to-shell transfer in the bottom panel (as we have written previously, what ought to be considered the closest to the standard Kolmogorov (1941) cascade probe, since all three interacting modes are \mathbf{u}_s) for each snapshot included in the averages (top row), as well as, $\langle u^2 \rangle_{\mathcal{V}}^{1/2}$ (non-dimensionalized by its time average in the steady state) as a function of t/t_0 . We probe only the steady state of evolution, derived previously from Figure 3. The black vertical lines indicate where each $\mathcal{T}(Q, K)$ was extracted from in the time series.

From the $\mathcal{T}_{ss}^s(Q_{\perp}, K_{\perp})$ transfer functions, it is immediately apparent that the nature and extent of the cascade change significantly over the span of a few $t_0 \sim 2.9$ Myr. For example, in the first realization, the left-most $\mathcal{T}_{ss}^s(Q_{\perp}, K_{\perp})$ shows a strongly truncated cascade, most likely from strong SNe detonating and disrupting the cascade (which happens just before the spike in $\langle u^2 \rangle_{\mathcal{V}}^{1/2}$; Kolborg et al. 2023). Compare this to the $\mathcal{T}_{ss}^s(Q_{\perp}, K_{\perp})$ second from the right, which has an extended cascade starting all the way from the lowest k modes during a low variability period in the evolution of $\langle u^2 \rangle_{\mathcal{V}}^{1/2}$.

It is not only the extent of the cascade that changes in time (i.e., which modes are participating in the cascade)

but also the strength of the non-local fluxes (i.e., the off-diagonal fluxes). In the first realization, one observes strong non-local energy transfers, which disappear almost completely by the next realization. To complicate matters even further, in the last realization, there appears to be a very weak and very local inverse cascade on some low- k modes, even for this completely incompressible transfer, \mathcal{T}_{ss}^s . This suggests that even the $\mathbf{u}_c \xrightarrow{u_c} \mathbf{u}_c$ mode interactions within our Galaxy may develop into complex energy flux behaviors (inverse versus direct, local versus non-local) that vary significantly in time. Specifically in more active (e.g., starburst) galaxies, the cascade may become strongly truncated on the large scales (even if one measures a power law in $\mathcal{P}_u(k)$ on those scales). Indeed, all of these features are simply not captured by the Kolmogorov (1941) phenomenology at all. Of course, we explore here only the hydrodynamics, and for a magnetized ISM this picture may only become more complicated. We leave the magnetized case for a future endeavor, but what we learn from our study is there are still a lot of unknowns to be discovered and made more precise, even in the hydrodynamical case.

6. WHAT FUELS THE INCOMPRESSIBLE CASCADES IN SUPERNOVA-DRIVEN TURBULENCE?

In Figure 7 we showed that \mathbf{u}_c interactions can transport energy from small scales to large scales, which can then be parasitized upon by low k modes through other flux transfers. Regardless of how efficient this process is, we need some way of turning \mathbf{u}_c modes generated by SNe into \mathbf{u}_s modes to fuel the incompressible cascades. As we derived in Section 5, the interaction that creates the $\mathbf{u}_s \rightarrow \mathbf{u}_s$ flux transfer is from $\mathbf{u} \cdot \mathbf{u} \cdot \nabla \otimes \mathbf{u}$. We can expand this term into two further terms, $\mathbf{u} \cdot \mathbf{u} \cdot \nabla \otimes \mathbf{u} = (1/2)\mathbf{u} \cdot \nabla u^2 - \mathbf{u} \cdot (\mathbf{u} \times \boldsymbol{\omega})$, where $\mathbf{u} \times \boldsymbol{\omega}$ is the Lamb vector. Hence, by exploring the $\boldsymbol{\omega}$ we are able to probe at least part of the turbulence generated via $\mathbf{u} \cdot \nabla \otimes \mathbf{u}$. The simplest way of determining $\boldsymbol{\omega}$ sources is by directly taking the curl of Equation 4. It is,

$$\frac{d\boldsymbol{\omega}}{dt} = \overbrace{-\boldsymbol{\omega}(\nabla \cdot \mathbf{u})}^{\text{compression}} + \underbrace{\boldsymbol{\omega} \cdot \nabla \otimes \mathbf{u}}_{\text{stretching}} + \overbrace{\frac{1}{\rho^2} \nabla \rho \times \nabla P}_{\text{baroclinicity}}, \quad (37)$$

where $d/dt = \partial_t + \mathbf{u} \cdot \nabla$ is the Lagrangian derivative, $\nabla \times \nabla \phi = 0$ by definition, and similarly, by definition, for the point-source supernova term in Equation 4.

The first term $\boldsymbol{\omega}(\nabla \cdot \mathbf{u})$ is the vortex compression term, which we associate with the post-shock regions from the supernova detonations. The third term $(1/\rho^2)\nabla \rho \times \nabla P$

is the baroclinic term, which is a battery term for $\boldsymbol{\omega}$, generated between misaligned pressure ∇P and gas density $\nabla \rho$ gradients. Misalignment may occur through interacting supernova shells, where the ∇P from one shell is not aligned with the $\nabla \rho$ from a neighboring shell, or even in the simpler case, where there is any obliqueness within a single expanding compressible wave (e.g., a corrugated shock wave or an expanding cooling layer), which is always the case. In fact, any kind of phase mixing may also excite the baroclinic term. This is similar to the Biermann battery effect (only the proportionality constant is different; McKee et al. 2020) for generating astrophysical magnetic fields in collisionless cosmic shocks (Biermann 1950). Finally, for an incompressible fluid, $\nabla \cdot \mathbf{u} = 0$, the second term $\boldsymbol{\omega} \cdot \nabla \otimes \mathbf{u}$ is the vortex stretching term, which we associate with vorticity structures interacting with a background shear flow. However, our fluid is highly compressible, and hence we must decompose $\nabla \otimes \mathbf{u}$ into components to extract only the (volume-preserving) stretching terms to make this equivalent to the incompressible vortex stretching operator (Schekochihin et al. 2004). Performing the same $\nabla \otimes \mathbf{u}$ decomposition as in Beattie et al. (2023a), the vorticity equation becomes

$$\frac{d\boldsymbol{\omega}}{dt} = -\frac{2\boldsymbol{\omega}}{3}(\nabla \cdot \mathbf{u}) + \boldsymbol{\omega} \cdot (\mathbb{S} + \mathbb{A}) + \frac{1}{\rho^2} \nabla \rho \times \nabla P, \quad (38)$$

$$\mathbb{S} = \frac{1}{2} (\nabla \otimes \mathbf{u} + [\nabla \otimes \mathbf{u}]^T) - \frac{1}{3} \mathbb{I} \nabla \cdot \mathbf{u}, \quad (39)$$

$$\mathbb{A} = \frac{1}{2} (\nabla \otimes \mathbf{u} - [\nabla \otimes \mathbf{u}]^T), \quad (40)$$

where \mathbb{S} and \mathbb{A} are the rate of strain and rate of rotation tensors, respectively, and $[\nabla \otimes \mathbf{u}]^T$ indicates the transpose. It is straightforward to show that \mathbb{A} only changes the unit vector of $\boldsymbol{\omega}$, since the enstrophy equation (for ω^2) gives rise to a term $\boldsymbol{\omega} \otimes \boldsymbol{\omega} : \mathbb{A}$, which is identically zero because $\boldsymbol{\omega} \otimes \boldsymbol{\omega}$ is a symmetric tensor and \mathbb{A} is antisymmetric, completely analogous to the turbulent dynamo process for a magnetic field embedded in a turbulent medium (Beattie et al. 2023a). Under this decomposition, the vortex compression term is modified to $-2\boldsymbol{\omega}(\nabla \cdot \mathbf{u})/3$, and the stretching term is simply $\sim \boldsymbol{\omega} \cdot \mathbb{S}$, no longer contaminated with compressions, and maintaining the vortex stretching definition as in the $\nabla \cdot \mathbf{u} = 0$ regime.

We measure the Equation 38 compression, stretching and baroclinic terms and show slices of the three-dimensional fields in Figure 10 and the time-evolution of the first moments in Figure 11. In Figure 10 we normalize all $\boldsymbol{\omega}$ terms by the volume integral rms value, revealing the underlying structure of the terms rather than the amplitudes, which we defer to Figure 11. Firstly,

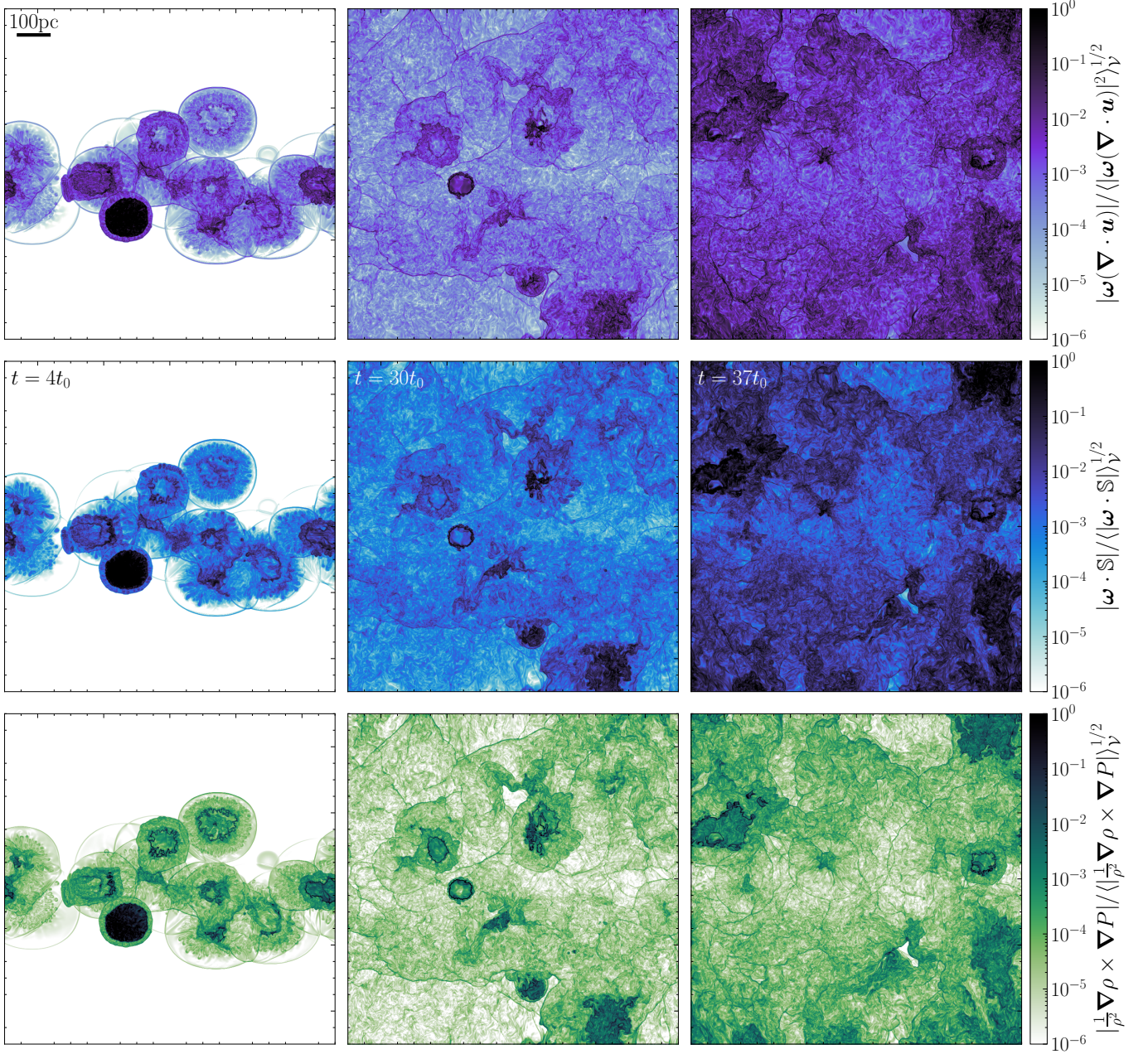


Figure 10. Similar to Figure 4, but each row corresponds to slices of the terms responsible for generating vorticity modes, $\partial_t \boldsymbol{\omega}$ (Equation 37), probing the generation of modes that participate in the incompressible turbulence cascade. **Top row:** vortex compression, $\sim \boldsymbol{\omega}(\nabla \cdot \mathbf{u})$. **Middle row:** vortex stretching, $\sim \boldsymbol{\omega} \cdot \mathbb{S}$, where \mathbb{S} is the rate of strain tensor (see Beattie et al. 2023a for why we use \mathbb{S} instead of the full $\nabla \otimes \mathbf{u}$). **Bottom row:** baroclinicity, $\sim \nabla \rho \times \nabla P$ the only battery term, in that it generates $\boldsymbol{\omega}$ without any initial seed $\boldsymbol{\omega}$. Each panel is normalized by the instantaneous rms value of the respective field, therefore these panels do not give information about the absolute values of each term (see Figure 11 for the rms amplitudes of each term), but emphasize the spacial structure of each individual component. All of the $\boldsymbol{\omega}$ generation terms are strongly correlated, mostly sensitive to the post-shock regions inside of the SNRs, and the SNe shock fronts themselves. However, in the $\nabla \rho \times \nabla P$ term, the most notable sources of $\boldsymbol{\omega}$ generation are the fractal cooling layers (e.g., Fielding et al. 2020) between the cold (exterior; $T \sim 10^4$ K) and hot (interior; $T \gtrsim 10^4$ K) gas in the SNRs.

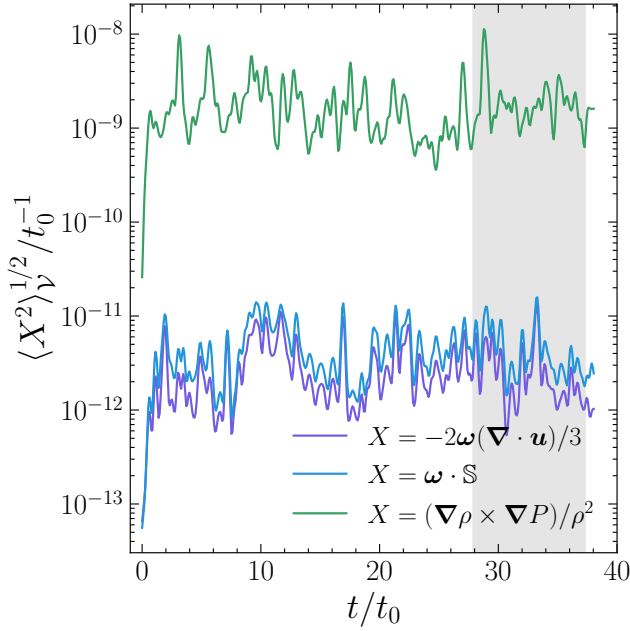


Figure 11. The same terms from Figure 10 but for the evolution of their rms normalized by t_0^{-1} . Throughout the entire evolution of the simulation the baroclinic term (green) dominates over the other two. During the steady state (shaded gray region) it is greater by approximately ~ 3 orders of magnitude, making it the leading order term in generating vorticity. Unlike the other two terms, baroclinicity generates vorticity without the need for any seed vorticity, hence can be completely fueled by compressible modes that source strong $\nabla\rho$ and ∇P misalignments through corrugated pressure and density interfaces (like fractal cooling layers, corrugated shocks, etc.) or interacting shock fronts.

it is clear that there is quite a strong correlation between all three terms, with intense ω generation in both post-shock regions and at the shock front in the SNe shells. In the early state $t \approx 4t_0$ (left panel), the generation of ω is concentrated on small scales, where the gas is less dense (see top left-panel in Figure 4, highlighting the stark contrast between the high-dense and low-dense components of the SNRs, potentially separated by the cooling radius; Martizzi et al. 2015, 2016). As the SNRs evolve beyond the Sedov-Taylor stage and into the snowplow stages (e.g., Martizzi et al. 2015), the shock front becomes a strong source of ω , with all terms (preferentially the $\sim \omega(\nabla \cdot \mathbf{u})$ term) showing significant ω generation around the boundary of the SNRs. By the time the turbulence becomes stationary, the ω generation spreads through the entire domain, but still with significant concentration in individual SNRs. Undoubtedly, all of the ω generation in the winds comes in part from the contribution of the inverse cascade discussed in Section 5.4 and shown in Figure 8.

The most distinct feature from these slices is that the baroclinic term is strongly enhanced at a particular corrugated surface within the SNRs. This is associated with a cooling layer that develops inside of each SNR, which is well-known to become highly-fractal and corrugated (Fielding et al. 2020; Lancaster et al. 2021, 2024, where Lancaster et al. (2021) has explored similar layers in the context of stellar winds). To show this explicitly, we plot temperature slices at the same t/t_0 as in the left column of Figure 10 in Figure 12. We specifically zoom in on the SNRs and reveal that indeed, the strong baroclinic source is the cooling layer between the hot $T > 10^4$ K that has been heated by the SNe explosion and the colder $T < 10^4$ K gas that cools as the SNRs expand. As Fielding et al. (2020) explains, these layers are already known to play an important role in facilitating the phase structure of the ISM. But now we also show, based on Figure 10 and Figure 12, they also end up being the strongest battery terms for vorticity in our ISM, and at a range of k associated with the fractal nature of the corrugation (e.g., a spectrum of \mathbf{u}_s modes, $u_s(k) \propto k^\beta$, where β is sourced directly from the fractal structure of the layer⁴, spontaneously generating the incompressible modes from the purely compressible modes driven by SNe detonations.

We show the rms of each term in Figure 11, revealing how the magnitude of each term varies as a function of t/t_0 . In steady state, indicated with the gray band (and even well before then) the ordering of the terms is $(1/\rho^2)\nabla\rho \times \nabla P \gg -2\omega(\nabla \cdot \mathbf{u})/3 \gtrsim \omega(\nabla \cdot \mathbf{u})$ in rms. Indeed, the baroclinic term is ~ 3 orders of magnitude larger than the other two terms. Hence, by taking the curl of both sides of Equation 38, using $\nabla \times \nabla \times \mathbf{u} = -\Delta\mathbf{u}$, where $\Delta = \partial_i\partial_i$ is the Laplacian, and by noting $\omega = \nabla \times \mathbf{u}_s$, to leading order,

$$\frac{d\mathbf{u}_s}{dt} = -\Delta^{-1}\nabla \times \left(\frac{1}{\rho^2}\nabla\rho \times \nabla P \right), \quad (41)$$

in our multiphase ISM, where Δ^{-1} is the inverse Laplacian. There may be analytical Green's function solutions to Equation 41, which we defer for future work that will require understanding local details about the cooling layers. Based on Figure 10 and Figure 12, we can confidently say that this is due to the intensely corrugated cooling layers inside the expanding SNRs, which can be seen even in the steady state (last two columns

⁴ Fielding et al. (2020) determined that $\mathcal{A}_\ell \propto \ell^{-1/2}$ for cooling layers of this kind, where \mathcal{A}_ℓ is the area of the layer on length scale ℓ . As Fielding et al. (2020) describes, Koch surfaces have the same $\mathcal{A}_\ell \propto \ell^{-1/2}$ scaling, indicating that the surface that produces ω is a complex, power-law structured field $[\nabla\rho \times \nabla P/\rho^2](\mathbf{k}) \sim \mathbf{k}^{-\alpha}$, that would generate an entire spectrum of modes in $\mathbf{u}_s(\mathbf{k})$.

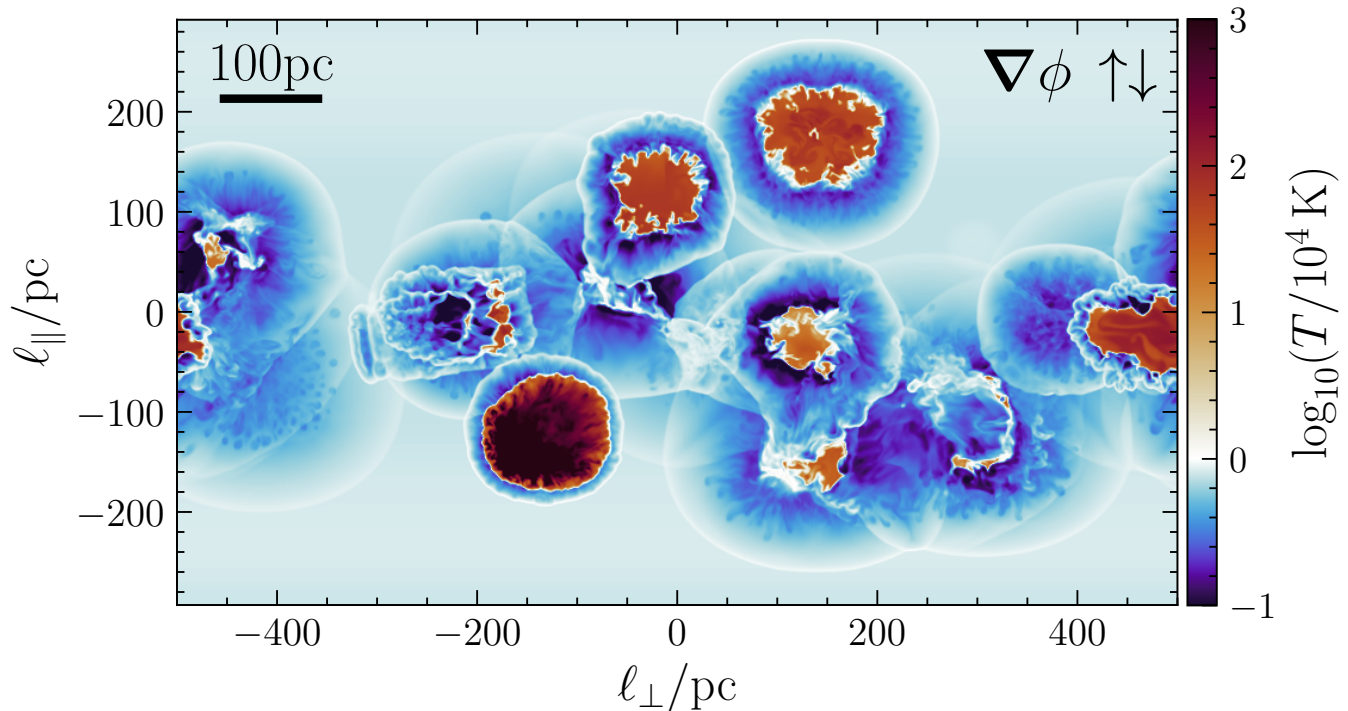


Figure 12. A two-dimensional logarithmic temperature (normalized by $T = 10^4$ K) slice of a zoom-in of the lower left panel in Figure 10, revealing that the baroclinic term, $\sim \nabla\rho \times \nabla P$, is the strongest at the fractal cooling layer between the hot $T > 10^4$ K plasma inside of the SNRs (shown in red) and the colder $T < 10^4$ K plasma outside of the SNRs (shown in blue). Because the baroclinic term dominates the total ω generation (Figure 11), this suggests that phase mixing through the fractal cooling layer is the strongest source of incompressible turbulence in the SNe-driven medium, and because the incompressible turbulence dominates the total energy in the turbulence (Figure 5), phase mixing is potentially the largest source of turbulence, in general.

in Figure 10). This is the main result from this section. This result is broadly consistent with previous baroclinic studies of SNe driven turbulence (Padoan et al. 2016) and other fluid simulations with non-isothermal EOS (Seta & Federrath 2022; Mohapatra et al. 2022), but here we make the result very explicit that it is the baroclinicity directly from the cooling layer embedded within the SNRs themselves that has the largest effect. Indeed, the cooling layers are likely candidates for why the \mathbf{u}_s modes were extremely energized within $k \gtrsim \ell_0^{-1}$ in the $\mathcal{P}_{u_c}(k)/\mathcal{P}_u(k)$ ratio in Figure 6.

This effect is a clear departure away from what can be captured in isothermal turbulent boxes, since $P \propto \rho$ isothermality implies that $|\nabla\rho \times \nabla P| = 0$, and here we find that it is three orders of magnitude larger than any other of the ω generation terms, contributing to strongly energizing the \mathbf{u}_s modes within the gaseous scale-height of the disk. Careful comparisons will need to be made to see if injecting \mathbf{u}_s modes through large-scale Fourier driving, as is standard practice, can compensate for the deficiency in \mathbf{u}_s modes that are absent when $|\nabla\rho \times \nabla P| = 0$. The top-left panel in (Federrath 2013, figure 8) suggests that for purely solenoidal driving, it indeed comes close (but potentially on the wrong

scales, as indicated in Figure 6). Moreover, this may be particularly concerning for simulations that are isothermal and driven with purely compressible modes, since there will be a lack of vorticity, in general, that may not be realized in a true multiphase ISM.

To close this section, let us briefly comment on an additional magnetized effect that is deeply tied to the $\nabla\rho \times \nabla P$, even though it is not present in the current simulation. As we pointed out in Section 6, the baroclinic vorticity battery sourced from the cooling layer term is proportional to the magnetic Biermann battery term (Biermann 1950; Harrison 1969; Kulsrud et al. 1997; McKee et al. 2020), i.e., $\partial_t \mathbf{b} \propto (\nabla\rho \times \nabla P)/\rho^2$ if $|b| = 0$. Indeed, the proportionality leads to a simple relation between \mathbf{b} and ω , which for a pressure gradient driven battery (e.g., Kulsrud et al. 1997) is,

$$|\mathbf{b}| = \frac{\bar{m}c}{(1 + \chi_i)e} |\omega|, \quad (42)$$

where \mathbf{b} is the magnetic field, $\bar{m} = \rho/\bar{n}$ is the mean mass of both the neutral and ionized atoms, $\bar{n} = n_i + n_n$ is the total number density, and $\chi_i = n_i/\bar{n}$ is the ionization fraction (McKee et al. 2020). For WIM parameters (Draine 2011; Beattie et al. 2022a), and using our value

for ω/t_0^{-1} from the baroclinic term in Figure 11 (where $t_0 \sim 3 \text{ Myr}$, Table 1), we find

$$b \sim 10^{-16} \left(\frac{t_0}{3 \text{ Myr}} \right) \left(\frac{\omega/t_0^{-1}}{10^{-9}} \right) \text{ G}, \quad (43)$$

providing a significant seed magnetic field over the k modes controlled by the fractal structure of the layer for the ISM which, following the incompressible modes, may ride up the inverse $\mathbf{u}_s \xrightarrow{\mathbf{u}_c} \mathbf{u}_s$ cascade to larger scales, being further enhanced by the turbulent dynamo, and magnetizing the winds and the surrounding medium (e.g., Tevlin et al. 2024). This is a strong seed magnetic field compared to the case where the vorticity is sourced from just turbulence alone, where $b \sim 10^{-19} \text{ G}$, as calculated in McKee et al. (2020), and consistent with substituting either $\omega(\nabla \cdot \mathbf{u})$ or $\omega \cdot \mathbb{S}$ into Equation 42, or generated on larger scales from cosmological shocks and ionization fronts $b \sim 10^{-19} - 10^{-21} \text{ G}$ (Zweibel 2013). This is yet another direct consequence of having an extremely strong source of baroclinicity in highly-corrugated cooling layers.

7. SUMMARY AND CONCLUSIONS

In this study, we perform a detailed analysis of the multiphase turbulence born from detonations of supernovae in a stratified disk undergoing cooling and heating through a time-dependent chemical network and the adiabatic expansions of the remnants. In particular, we focus a lot of our efforts on the transfer of kinetic energy flux through the nonlinear advection term $u_i u_j \partial_j u_i$ in the momentum equation, which defines both the compressible and incompressible mode turbulence cascades. We do this using energy flux transfer functions, which allow us to compute all three mode interactions in $u_i u_j \partial_j u_i$, split into incompressible \mathbf{u}_s and compressible \mathbf{u}_c modes. In this summary, we will focus on synthesizing the physical picture that has emerged from the analysis of our simulation for how supernova-driven turbulence works in a disk of a galaxy. This will have missing physics, such as rotation, magnetized turbulence and dynamo, and cold plasma phases, but our main goal was always to gather a simple physical picture of supernova-driven turbulence, which we hope can help understand the nature of the turbulence in our own Galaxy.

7.1. A supernova-driven turbulence phenomenology

Let us put together everything that we have learnt in this study into a coherent narrative for the nature of SNe-driven turbulence. SNe-driven turbulence injects compressible modes, \mathbf{u}_c , on the smallest scales in the system, i.e., it is compressibly-driven turbulence. As the

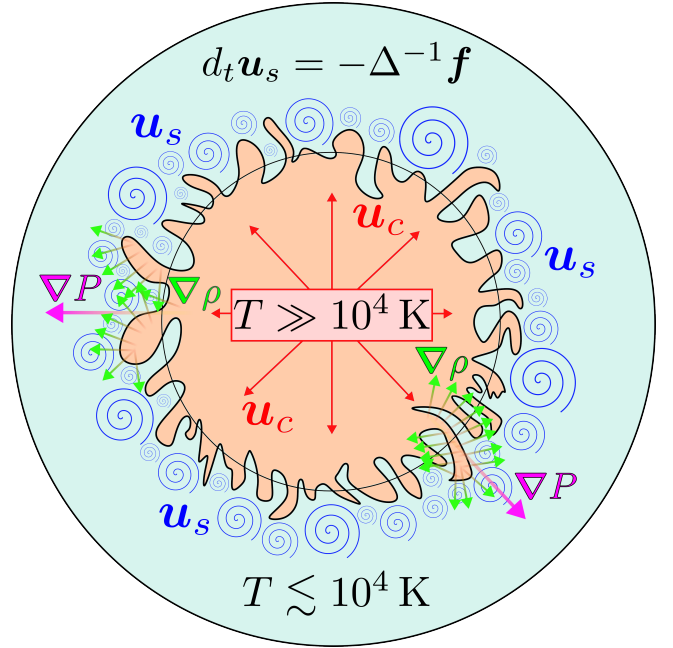


Figure 13. A schematic summarizing the incompressible \mathbf{u}_s mode (blue) generation through the corrugated cooling layer (black) between the hot (orange) and warm (teal) gas, which are stretched to larger scales by the compressible \mathbf{u}_c modes (red) associated with the expanding SNRs. The cooling layer generates a large spectrum of \mathbf{u}_s modes due to the fractal nature of the layer (see Fielding et al. 2020, for the fractal characterization of such a layer). The rate in which the baroclinic term generates \mathbf{u}_s modes admits to the Green’s function solution where $\mathbf{f} = \nabla \times (\nabla \rho \times \nabla P / \rho^2)$, Equation 41, where examples of the ∇P for the layer is shown in pink, and the $\nabla \rho$ or the layer in green.

SNe detonate they heat the gas to $T \gg 10^4 \text{ K}$ and as they expand into the WIM ($T \sim 10^4 \text{ K}$) they cool adiabatically, creating corrugated cooling layers. Due to the corrugation, $|\nabla \rho \times \nabla P| \gg 1$, which intensely generates incompressible, vortical modes, \mathbf{u}_s , across a broad spectrum of k modes determined by the fractal nature of the layer (see Figure 13). These modes energize the scales below the gaseous scale height, ℓ_0 , such that almost 90% of the energy is in \mathbf{u}_s . The expanding SNRs facilitates an inverse cascade via the three-mode interaction, $\mathbf{u}_s \xrightarrow{\mathbf{u}_c} \mathbf{u}_s$, that brings \mathbf{u}_s modes up to scales well beyond ℓ_0 , e.g., into the galactic winds and throughout the disk. At the same time, the post-shock regions have relatively local, direct cascades, $\mathbf{u}_s \xrightarrow{\mathbf{u}_s} \mathbf{u}_s$, that transport energy flux down to smaller scales. On the large scales, the $\mathbf{u}_s \xrightarrow{\mathbf{u}_s} \mathbf{u}_s$ cascade is highly non-local, with \mathbf{u}_s modes more or less coupling across all scales, meaning energy from \mathbf{u}_s is deposited directly from the large scales (1 kpc) to the small scales (10 pc), without undergoing a Kolmogorov (1941)-style cascade. The compressible modes from the expanding SNRs interact

with one another through the three-mode interaction $\mathbf{u}_c \xrightarrow{\mathbf{u}_c} \mathbf{u}_c$, which gives rise to a relatively non-local direct transfer of energy from large to small scales, perhaps resembling the non-local Burgers (1948)-type turbulence. However, there is a \mathbf{u}_c cascade that is very local across all scales through the $\mathbf{u}_c \xrightarrow{\mathbf{u}_s} \mathbf{u}_c$ interaction, perhaps scattering the \mathbf{u}_c modes down the \mathbf{u}_s -dominated galactic winds and post-shocked regions. By this time, fully developed turbulent spectra have been established in the medium, albeit with significant time variability associated with the strong SNe detonation events. The spectra are $\mathcal{P}_{u_c}(k) \sim k^{-2}$ for the compressible modes and $\mathcal{P}_{u_s}(k) \sim k^{-3/2}$ for the incompressible. Over the range of scales for which these power laws hold, the \mathbf{u}_c modes are undergoing both local $\mathbf{u}_c \xrightarrow{\mathbf{u}_s} \mathbf{u}_c$ and non-local $\mathbf{u}_c \xrightarrow{\mathbf{u}_c} \mathbf{u}_c$ cascades, whereas the \mathbf{u}_s modes are undergoing $\mathbf{u}_s \xrightarrow{\mathbf{u}_c} \mathbf{u}_s$ inverse and $\mathbf{u}_s \xrightarrow{\mathbf{u}_s} \mathbf{u}_s$ non-local cascades. Hence, neither of the incompressible cascades in SNe-driven turbulence is consistent with the Kolmogorov (1941) phenomenology of turbulence.

Finally, it is worth highlighting that in the phenomenology we have drawn out, whether it be by bringing energy from the small-to-large-scales via an inverse cascade, or generating vorticity via the baroclinic term, the compressible modes play a critical and vital role in a SNe-driven medium, and are not passive in any of the processes, which has been the conventional wisdom of the magnetohydrodynamic ISM community (Lithwick & Goldreich 2001). Indeed, our results suggest that the multiphase ISM turbulence ecosystem relies critically on both the incompressible and compressible modes playing different but very important roles in creating and maintaining the turbulent fluctuations and cascades.

We now itemize some of the key results from this study:

- We drive a stratified ISM into stationarity with SNe detonations happening at the grid scale, resulting in $\mathcal{M} = 1.75 \pm 0.05$ (Figure 3). The SNe and our time-dependent cooling network give rise to a multiphase ISM, with a cooling floor at $T \approx 10^4$ K (Figure 2). However, the plasma is able to cool to $\lesssim 10^2$ K through the adiabatic expansion of the SNRs, as shown with the blue adiabat in Figure 2. Based on the velocity dispersion, $\langle u^2 \rangle_V^{1/2} = 28 \pm 6$ km s $^{-1}$, and gaseous scale-height, $\ell_0 = 85 \pm 6$ pc, we calculate a turbulent turnover time on ℓ_0 as $t_0 = 2.9$ Myr.
- We decompose the velocity field into incompressible \mathbf{u}_s and compressible \mathbf{u}_c modes using the Helmholtz Decomposition, and with this directly calculate cylindrically ($\ell_{\parallel}, \ell_{\perp}$, with respect to the

gravitational potential, $\nabla\phi$) summed energy spectra $\mathcal{P}_u(k)$ for each type of mode (Figure 5). We find $\mathcal{P}_{u_s}(k) \sim k^{-3/2}$ and $\mathcal{P}_{u_c}(k) \sim k^{-2}$, regardless of the direction, indicating that the turbulence is rather isotropic. By computing the ratio between the spectra we find that the turbulence is everywhere dominated by \mathbf{u}_s modes, and particularly on modes $k > \ell_0^{-1}$, i.e., on scales below the scale-height, where \mathbf{u}_s is more dominant than what even local turbulent boxes driven completely with solenoidal modes can achieve. We show that the correlation scales of the turbulence are $\sim 4\ell_0$, indicating that the turbulence is correlated well into the galactic winds.

- Using spectral transfer functions for the \mathbf{u}_c and \mathbf{u}_s kinetic flux we investigate four different cascades in two different directions generated from the $u_i u_j \partial_j u_i$ nonlinearity (Equation 28-Equation 31), shown via shell-to-shell transfers in Figure 7. Similar to the power spectrum, there is not a significant difference between the two directions. The $\mathbf{u}_c \xrightarrow{\mathbf{u}_s} \mathbf{u}_c$ is a highly-local, direct cascade, $\mathbf{u}_c \xrightarrow{\mathbf{u}_c} \mathbf{u}_c$ is a more non-local, direct cascade, potentially due to a mechanism like Burgers (1948)-type turbulence. $\mathbf{u}_s \xrightarrow{\mathbf{u}_s} \mathbf{u}_s$ is a highly non-local, direct cascade, specifically at scales where $\mathcal{P}_{u_s}(k) \sim k^{-3/2}$ and $\mathbf{u}_s \xrightarrow{\mathbf{u}_c} \mathbf{u}_s$ is a mixture of inverse cascade on the scales where $\mathcal{P}_{u_s}(k) \sim k^{-3/2}$ and a direct cascade at smaller scales. The cascade varies significantly in total energy flux, length and even direction when sampled across multiple realizations in the steady state (Figure 9).
- By visualizing the energy flux everywhere in space (Figure 8) we reveal that there are simultaneous inverse and direct cascades happening everywhere in the $\mathbf{u}_s \xrightarrow{\mathbf{u}_c} \mathbf{u}_s$ transfer of energy flux. Specifically, we identify strong sources of inverse cascades as expanding SNRs that advect \mathbf{u}_s modes to lower k , larger ℓ , energizing \mathbf{u}_c modes in the winds, beyond the gaseous scale height of the disk.
- We further show that the dominant source of incompressible modes in SNe-driven turbulence is from baroclinicity in fractal cooling layers in the SNRs (Figure 10 and Figure 11). This is the corrugated layer between the hot, $T \gtrsim 10^4$ K SNR interior and warm $T \sim 10^4$ K surrounding ISM, shown very clearly in Figure 12. We hypothesize that the cooling layer generates the \mathbf{u}_s modes that are then taken to the large scales through the $\mathbf{u}_s \xrightarrow{\mathbf{u}_c} \mathbf{u}_s$ inverse cascade mechanism, which contributes to

feeding \mathbf{u}_s modes into the winds and also the direct cascades. We use the measured ω/t_0^{-1} and WIM plasma parameters to directly estimate the Biermann field that the cooling layer would generate (Equation 42), which is 10^{-16} G – strong seed magnetic field that could contribute to magnetizing the galaxy and surrounding medium when coupled to other processes, like the turbulent dynamo.

ACKNOWLEDGMENTS

We thank Philipp Grete for the useful comments that allowed us to find a bug in our original transfer functions. We also thank Mark Krumholz for the helpful comments about the warm ISM phases. J. R. B. acknowledges financial support from the Australian National University, via the Deakin PhD and Dean’s Higher Degree Research (theoretical physics) Scholarships and the Australian Government via the Australian Government Research Training Program Fee-Offset Scholarship and the Australian Capital Territory Government funded Fulbright scholarship, which facilitated this collaboration and project. J. R. B. further acknowledges the support from NSF Award 2206756, and compute allocations rrg-ripperda from the Digital Research Alliance of Canada, as well as high-performance computing resources provided by the Leibniz Rechenzentrum and the Gauss Center for Supercomputing grant pn76gi pr73fi and pn76ga. A. N. K. and E. R.-R. acknowledge support by the Heising-

Simons Foundation, the Danish National Research Foundation (grant No. DNRF132) and the NSF (grant Nos. AST-2206243, AST-1911206, and AST-1852393). C. F. acknowledges funding provided by the Australian Research Council (Discovery Project grants DP230102280 and DP250101526), and the Australia-Germany Joint Research Cooperation Scheme (UADAA). C. F. further acknowledges high-performance computing resources provided by the Leibniz Rechenzentrum and the Gauss Centre for Supercomputing (grant pr32lo), the Australian National Computational Infrastructure (grant ek9) and the Pawsey Supercomputing Centre (project pawsey0810) in the framework of the National Computational Merit Allocation Scheme and the ANU Merit Allocation Scheme.

Facilities: This research was undertaken with the assistance of resources from the National Computational Infrastructure (NCI Australia), an NCRIS enabled capability supported by the Australian Government.

Software: Data analysis and visualization software used in this study: C++ (Stroustrup 2013), NUMPY (Oliphant 2006; Harris et al. 2020), NUMBA, (Lam et al. 2015), MATPLOTLIB (Hunter 2007), CYTHON (Behnel et al. 2011), VISIT (Childs et al. 2012), SCIPY (Virtanen et al. 2020), SCIKIT-IMAGE (van der Walt et al. 2014), CMASHER (van der Velden 2020), YT (Turk et al. 2011), PANDAS (pandas development team 2023), JOBLIB (Joblib Development Team 2020)

APPENDIX

A. MIXED MODE SHELL-TO-SHELL TRANSFERS FUNCTIONS

We compute a total of 20 transfer functions, as discussed in Section 5. The main text included only like-mode transfers, $\mathbf{u}_s \rightarrow \mathbf{u}_s$, $\mathbf{u}_c \rightarrow \mathbf{u}_c$, which probe the energy flux directly related to the spectrum we show in Figure 5. However, there are the mixed mode combinations that we did not show in the main text, $\mathbf{u}_s \leftrightarrow \mathbf{u}_c$, which describe the energy flux transfer between \mathbf{u}_s and \mathbf{u}_c , relating to the exchange of energy flux between the two spectra. One can also think of these transfer functions as probing the amount of \mathbf{u}_c modes turning into \mathbf{u}_s modes, and vice-versa. The transfer functions that describe these processes are

$$\begin{aligned} \mathbf{u}_s \xrightarrow{\mathbf{u}_c} \mathbf{u}_c, & & \mathbf{u}_c \xrightarrow{\mathbf{u}_c} \mathbf{u}_s, \\ \mathcal{T}_{sc}^c(Q, K) = - \int d^3\ell \mathbf{u}_c^K \otimes \mathbf{u}_c : \nabla \otimes \mathbf{u}_s^Q, & & \mathcal{T}_{cs}^c(Q, K) = - \int d^3\ell \mathbf{u}_s^K \otimes \mathbf{u}_c : \nabla \otimes \mathbf{u}_c^Q, \end{aligned} \quad (\text{A1})$$

$$\begin{aligned} \mathbf{u}_s \xrightarrow{\mathbf{u}_s} \mathbf{u}_c, & & \mathbf{u}_c \xrightarrow{\mathbf{u}_s} \mathbf{u}_s, \\ \mathcal{T}_{sc}^s(Q, K) = - \int d^3\ell \mathbf{u}_c^K \otimes \mathbf{u}_s : \nabla \otimes \mathbf{u}_s^Q, & & \mathcal{T}_{cs}^s(Q, K) = - \int d^3\ell \mathbf{u}_s^K \otimes \mathbf{u}_s : \nabla \otimes \mathbf{u}_c^Q. \end{aligned} \quad (\text{A2})$$

We show the shell-to-shell transfers in Figure 14, organized in a similar way as our cascade shell-to-shell transfers Figure 7. As was the case in the cascade transfers, there is no significant difference between ℓ_\perp and ℓ_\parallel , so we focus our discussion on each mixed transfer. Firstly, there are no strict cascades in any of these transfers (local and diagonally dominated), which makes sense since these transfers probe the flux between \mathbf{u}_c and \mathbf{u}_s cascades. The \mathbf{u}_s -mediated

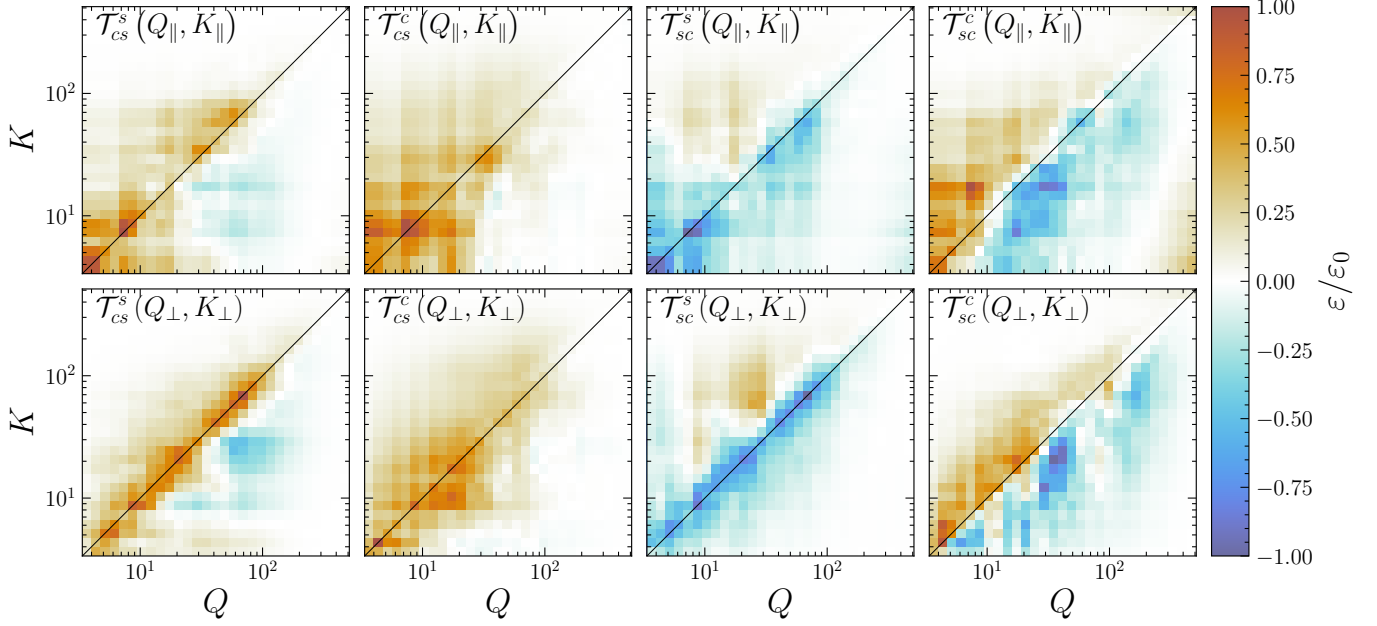


Figure 14. Same as Figure 7 but for mixed mode shell-to-shell transfers, $\mathbf{u}_c \leftrightarrow \mathbf{u}_s$, Equation A1-Equation A2.

transfers have good anti-symmetry $\mathcal{T}_{cs}^s(Q, K) = -\mathcal{T}_{sc}^s(K, Q)$, but the \mathbf{u}_c -mediated transfers do not, which we explain in Appendix C. Both \mathcal{T}_{cs}^s and \mathcal{T}_{sc}^s show that \mathbf{u}_c modes donate energy to \mathbf{u}_s modes, across quite a broad range of k when mediated by either \mathbf{u}_c or \mathbf{u}_s . The same is true for the \mathcal{T}_{cs}^c transfer, has $\varepsilon > 0$ on all k modes, but especially at low- k , showing that $\mathbf{u}_c \rightarrow \mathbf{u}_s$ on large scales when mediated by an additional \mathbf{u}_c mode. However, the \mathcal{T}_{sc}^c transfer shows a mix of \mathbf{u}_s modes turning back into \mathbf{u}_c modes (red, in the upper diagonal) and \mathbf{u}_c modes turning into \mathbf{u}_s modes (blue). What we learn is that the flux preferentially goes from $\mathbf{u}_c \rightarrow \mathbf{u}_s$, and this happens at most k , but with a small preference for lower k when mediated by \mathbf{u}_c .

B. CROSS SCALE ENERGY FLUX AND TOTAL FLUX AMPLITUDE OF CASCADE TRANSFERS

In Section 5.3 we analyzed the energy transfer between individual k mode shells, Q and K . However, following Grete et al. (2017b), here we consider the cross-scale energy transfer $\Pi(k)$, and the total flux amplitude, Π_0 , of each transfer function. They are defined

$$\Pi(k) = \sum_{Q \leq k} \sum_{K > k} \mathcal{T}_{ii}^j(Q, K), \quad \Pi_0 = \sum_{k_{\text{inertial}}} \Pi(k), \quad (\text{B3})$$

which is the total energy flux from all Q shells smaller than k , to all K shell modes larger than k . We use this statistic to define an inertial range, k_{inertial} , where $\varepsilon \approx \text{const.}$ (very approximately), 'a la Kolmogorov, and then define the total cross-scale transfer, Π_0 , by simply summing over $\Pi(k)$ in the inertial range k_{inertial} . We use Π_0 to normalize all transfers (both cross and shell-to-shell; Section 5) throughout the study, and use the k_{inertial} derived to indicate where the inertial range is for Figure 5 and Section 4.

We show the cross-scale transfer function for the cascade mode transfers in Figure 15 and mixed mode transfers in Figure 16. Firstly, we note that the energy flux does not become completely constant at any range of k . However, there is a small range of k in the isolated transfers, \mathcal{T}_{cc}^c and \mathcal{T}_{ss}^s that is constant within the 1σ fluctuations. We indicated where this region is with the gray bands, and this is the region we call the inertial range. Note that the \mathcal{T}_{cc}^c and \mathcal{T}_{ss}^s fluxes dominate the total energy flux, showing that these two cascades (both quite non-local transfers, see Figure 7) are the most efficient at moving energy through the different modes. The mixed mode transfers shown in Figure 16 have a factor of two smaller flux. Hence, the \mathcal{T}_{cc}^c and \mathcal{T}_{ss}^s cascades are significantly more efficient at pushing energy down the cascade than the mode interactions between the cascades are at exchanging energy.

Finally, in Figure 17 we plot the total summed energy flux in the inertial range indicated by Figure 15. We normalized all the fluxes by the total across all transfers, such that the first two columns sum to one, $\mathcal{T}_{uu}^s + \mathcal{T}_{uu}^c = 1$, and so do

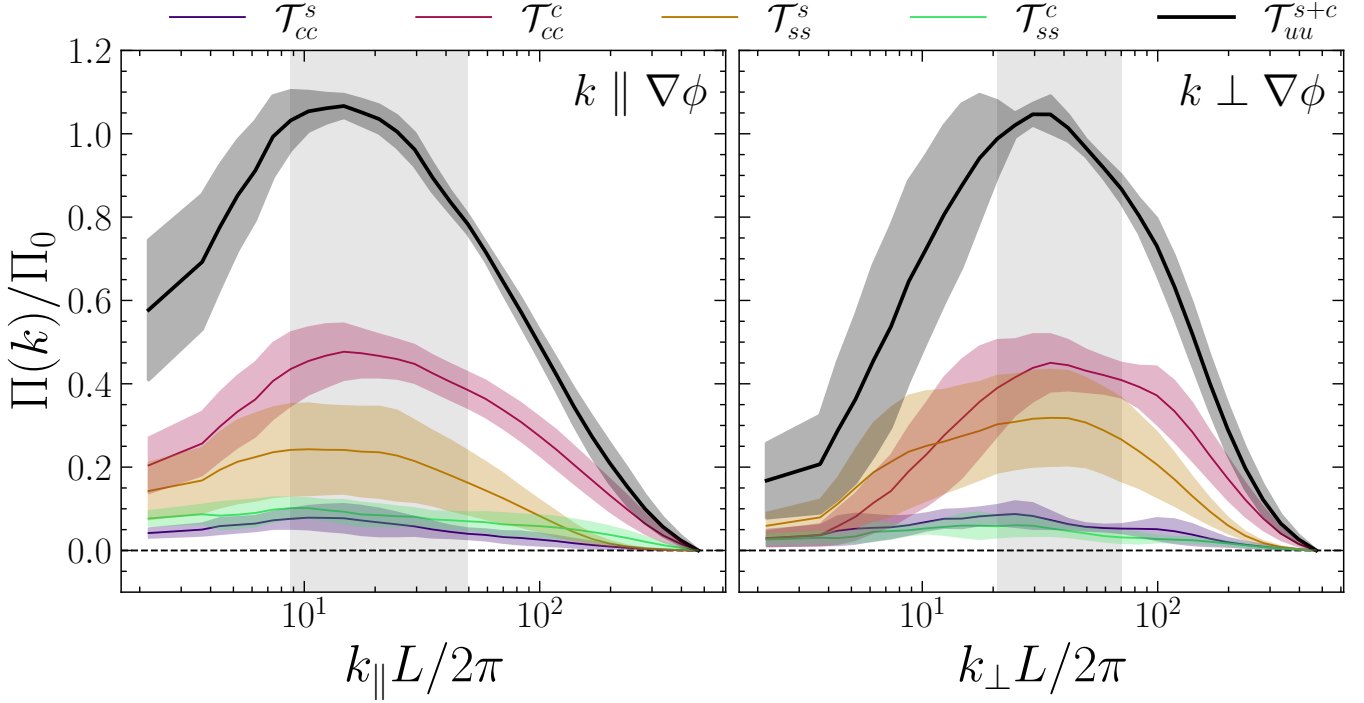


Figure 15. Cross scale transfer, $\Pi(k)/\Pi_0$ (Equation B3), for like-mode ($\mathbf{u}_c \rightarrow \mathbf{u}_c$ or $\mathbf{u}_s \rightarrow \mathbf{u}_s$; Equation 28 to Equation 31) and total mode interactions, normalized by the cross scale transfer in the \sim inertial range, Π_0 (shaded black region, based on the classical assumption for Kolmogorov (1941)-type turbulence, $\Pi(k)/\Pi_0 = \text{const.}$) along (k_{\parallel} ; top panel) and across (k_{\perp} ; bottom panel) the $\nabla\phi$. Colored, shaded bands on each $\Pi(k)/\Pi_0$ curve denote the 1σ time variation. The flux from three like-mode interactions (either all \mathbf{u}_c or all \mathbf{u}_s) dominate the energy flux, and show the closest behavior to the expected $\Pi(k)/\Pi_0 = \text{const.}$ across a small range of wavenodes in the simulations.

the next eight columns, $\mathcal{T}_{cc}^s + \mathcal{T}_{cc}^c + \mathcal{T}_{ss}^s + \mathcal{T}_{ss}^c + \mathcal{T}_{cs}^s + \mathcal{T}_{cs}^c + \mathcal{T}_{sc}^s + \mathcal{T}_{sc}^c = 1$. The \mathbf{u}_c mode-mediated transfers have the largest energy flux, which is dominated by the \mathcal{T}_{cc}^c transfer.

C. ANTISYMMETRIC PROPERTY OF HELMHOLTZ DECOMPOSED TRANSFER FUNCTIONS

In general, transfer functions should have the antisymmetric property,

$$\mathcal{T}(Q, K) = -\mathcal{T}(K, Q), \quad (\text{C4})$$

and in this section we shall explore this property for the Helmholtz decomposed transfers, focusing, as we have done for the entire study, just on the $\mathbf{u} \otimes \mathbf{u} : \nabla \otimes \mathbf{u}$ nonlinearity. Consider the classical turbulence cascade term that we use to explore the cascade in Section 5,

$$-\int_{\mathcal{V}} d\mathcal{V} u_i^K u_j \partial_j u_i^Q = \int_{\mathcal{V}} d\mathcal{V} \partial_j (u_i^K u_j u_i^Q) + \int_{\mathcal{V}} d\mathcal{V} u_i^K u_i^Q \partial_j u_j + \int_{\mathcal{V}} d\mathcal{V} u_j u_i^Q \partial_j u_i^K, \quad (\text{C5})$$

from the product rule, written in tensorial form. Using the divergence theorem,

$$\int_{\mathcal{V}} d\mathcal{V} \partial_j (u_i^K u_j u_i^Q) = \oint_{\partial\mathcal{V}} u_i^K u_j u_i^Q d\partial\mathcal{V}_j = 0, \quad (\text{C6})$$

if the domain is periodic. In our case, we have only doubly-periodic boundaries, so this surface integral will not be exactly zero. However, based on the antisymmetry that is preserved in the incompressible mediated transfer functions (see Figure 7), seemingly this has a very small effect. Then,

$$-\int_{\mathcal{V}} d\mathcal{V} u_i^K u_j \partial_j u_i^Q = \int_{\mathcal{V}} d\mathcal{V} u_i^K u_i^Q \partial_j u_j + \int_{\mathcal{V}} d\mathcal{V} u_j u_i^Q \partial_j u_i^K. \quad (\text{C7})$$

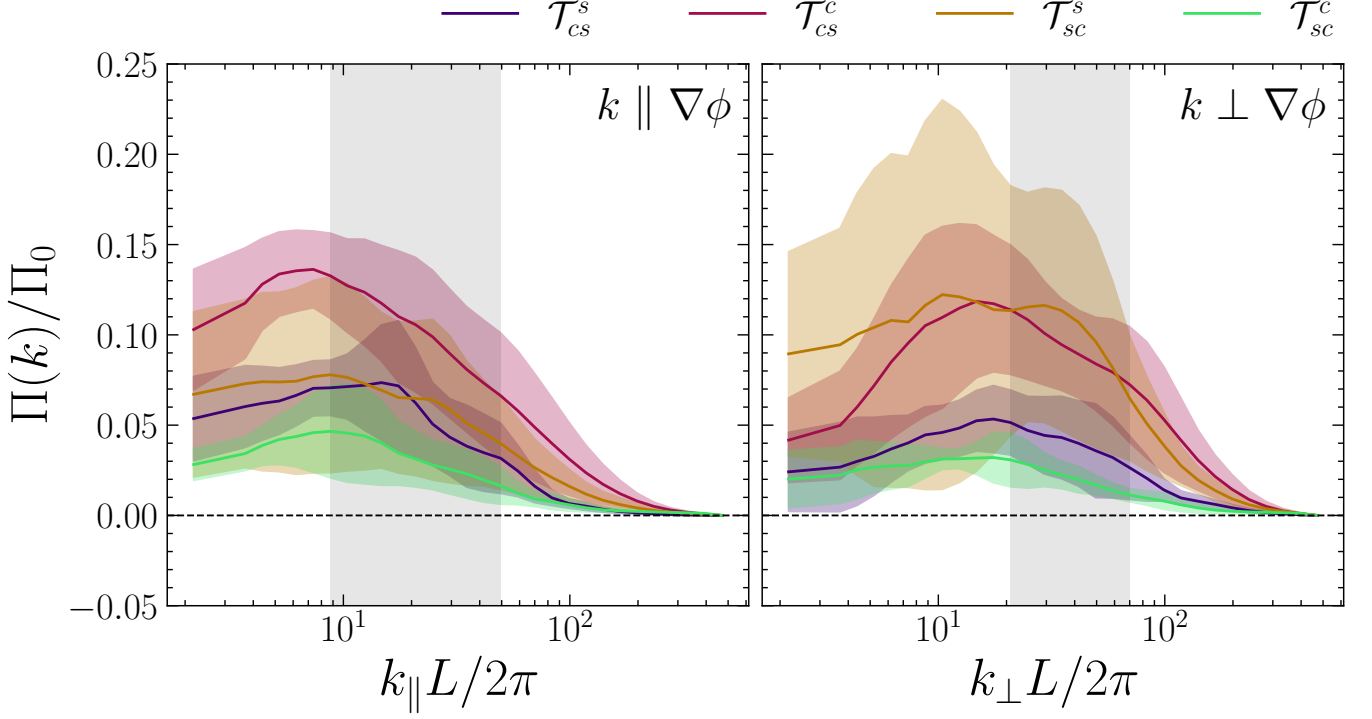


Figure 16. The same as figure Figure 15 but for mixed mode cross scale transfers, $u_c \rightarrow u_s$ and $u_s \rightarrow u_c$.

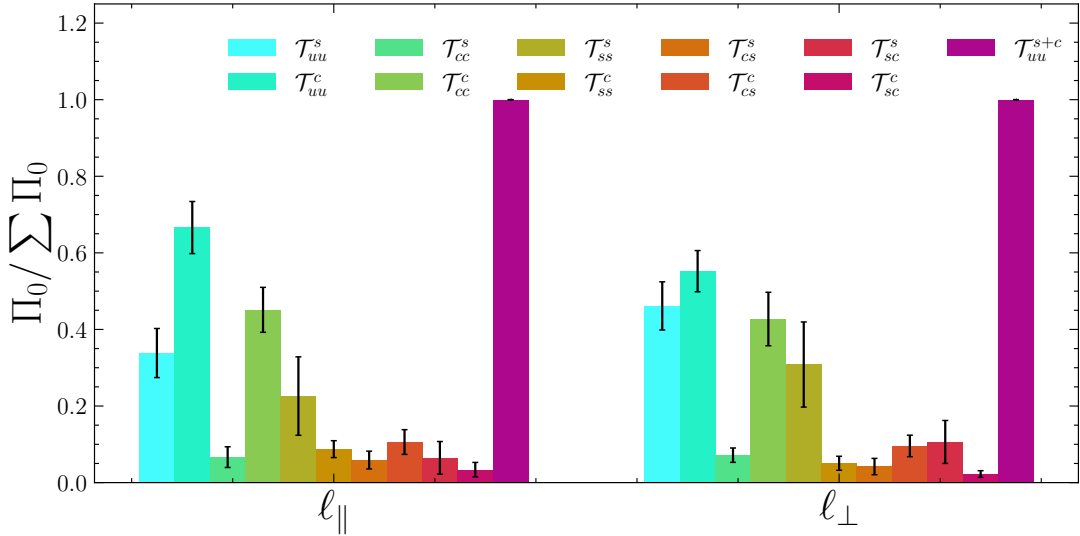


Figure 17. The integrated energy flux contributions from each of the transfers integrated in the range of scales in the inertial range k_{inertial} (gray bands in Figure 15 and Figure 16). All transfers are normalized by the energy flux of the total transfer function \mathcal{T}_{uu}^u (last bar), such that the $\mathcal{T}_{uu}^s + \mathcal{T}_{uu}^c = 1$ (first two bars) and then the remaining eight transfers, $\mathcal{T}_{cc}^s + \mathcal{T}_{cc}^c + \mathcal{T}_{ss}^s + \mathcal{T}_{ss}^c + \mathcal{T}_{cs}^s + \mathcal{T}_{cs}^c + \mathcal{T}_{sc}^s + \mathcal{T}_{sc}^c = 1$. The cascade flux \mathcal{T}_{cc}^c dominates the energy flux, followed by \mathcal{T}_{ss}^s .

Now consider the compressible u_i^c and incompressible u_i^s mode decomposition that we perform throughout Section 5. Without loss of generality, if we consider only the mediating mode, for the compressible mode we have

$$-\int_{\mathcal{V}} dV u_i^K u_j^c \partial_j u_i^Q = \int_{\mathcal{V}} dV u_i^K u_i^Q \partial_j u_j^c + \int_{\mathcal{V}} dV u_j^c u_i^Q \partial_j u_i^K, \quad (\text{C8})$$

and for incompressible,

$$-\int_{\mathcal{V}} d\mathcal{V} u_i^K u_j^s \partial_j u_i^Q = \int_{\mathcal{V}} d\mathcal{V} u_j^s u_i^Q \partial_j u_i^K. \quad (\text{C9})$$

This means that transfer functions mediated by u_i^s are antisymmetric with themselves, as is expected from regular incompressible transfer function theory (Alexakis et al. 2005), but transfer functions mediated by u_i^c are not. From Equation C8, they are instead antisymmetric with the total velocity transfer function,

$$\mathcal{T}^c(Q, K) = - \int d^3\ell [\mathbf{u}^K \otimes (\mathbf{u}_c : \nabla \otimes \mathbf{u}^Q + \mathbf{u}^Q : (\nabla \cdot \mathbf{u}_c)\mathbb{I})], \quad (\text{C10})$$

which we do not investigate in this study, due to the fact that the antisymmetric component of a transfer function we are already computing does not contain any further information. However, this does explain why all of the $\mathcal{T}^c(Q, K)$ transfer functions are not antisymmetric with themselves, whereas the $\mathcal{T}^s(Q, K)$ transfers are.

D. KINETIC HELICITY

The kinetic helicity, $\mathcal{H}_{\text{kin}} = \langle \boldsymbol{\omega} \cdot \mathbf{u} \rangle_{\mathcal{V}}$, describes the volume-averaged asymmetry in the left versus right eigenmodes of \mathbf{u}_s in the fluid (clockwise orientated $\boldsymbol{\omega}_+$ versus anticlockwise orientated $\boldsymbol{\omega}_-$; Alexakis 2017; Plunian et al. 2020). If $|\langle \boldsymbol{\omega} \cdot \mathbf{u} \rangle_{\mathcal{V}}| \gtrsim 0$ then we expect there to be an excess of left or right modes, which, when interacting, $\boldsymbol{\omega}_{\pm} \rightarrow \boldsymbol{\omega}_{\pm}$, have, on average, an energy flux from small to large scales, $\varepsilon < 0$. Hence, $\boldsymbol{\omega}_+ \rightarrow \boldsymbol{\omega}_+$ or $\boldsymbol{\omega}_- \rightarrow \boldsymbol{\omega}_-$ velocity mode interactions can give rise to an inverse cascade, as demonstrated utilizing $\boldsymbol{\omega}_{\pm}$ transfer functions in three-dimensional hydrodynamic turbulence driven with net kinetic helicity (Alexakis 2017; Plunian et al. 2020). In our study, we show that the $\mathbf{u}_s \rightarrow \mathbf{u}_s$ mediated by \mathbf{u}_c interaction can also provide a mechanism for inverse transfer. Therefore, a natural question is the nature of the handedness of $\mathbf{u}_s \rightarrow \mathbf{u}_s$ transfers during this interaction. We leave the details of this for a future study, where we intend to track both eigenmodes, but we provide \mathcal{H}_{kin} as a function of t/t_0 for the 512³ simulation to at least understand if the supernova-driven turbulence becomes net helical (note that \mathcal{H}_{kin} is no longer an invariant in compressible hydrodynamics, so small helicity fluctuations could indeed grow).

We show the kinetic helicity in Figure 18, where for all time the supernova-driven turbulence is completely non-helical (in volume average) $|\langle \boldsymbol{\omega} \cdot \mathbf{u} \rangle_{\mathcal{V}}| \approx 0$, at least to single precision. We also show a two-dimensional slice of the point-wise kinetic helicity $\boldsymbol{\omega} \cdot \mathbf{u}$ normalized by the rms, Figure 19, with the same annotations as in Figure 12. This is early in the evolution of the simulation, just to easily visualize what is happening in and around the SNRs, but no conclusions change in the steady state. What we observe are strong $\boldsymbol{\omega} \cdot \mathbf{u}$ fluctuations, localized around the SNRs. The signed fluctuations become comparable to the size of the typical size of the SNRs, significantly larger than the background fluctuations in the disk. Furthermore, they are bright, indicating that the fluctuations contain strong alignment between \mathbf{u} and $\boldsymbol{\omega}$. This suggests, like $\mathbf{u}_s \xrightarrow{u_c} \mathbf{u}_s$ interactions, the \mathbf{u}_c modes generated in the SNRs take strong $\boldsymbol{\omega} \cdot \mathbf{u}$ fluctuations to large scales. As previously discussed in Käpylä et al. (2018), this is important for large-scale, stochastic α dynamos (Rincon 2019). So even though $\mathcal{H}_{\text{kin}} \approx 0$, the fluctuations in $\boldsymbol{\omega} \cdot \mathbf{u}$ may still be important for both the ISM dynamo and the handed interactions in the turbulence.

E. CONVERGENCE TEST

In order to test the convergence of our results, we calculate the total velocity power spectra, $\mathcal{P}_u(k)$ for all three resolutions (MW_256, MW_512, MW_1024; see Table 1) runs included in this study, shown in Figure 5. As in Section 4, we normalize each spectrum by its respective integral, i.e., $\langle u^2 \rangle_{\mathcal{V}}$, by Parseval's theorem. For both k_{\parallel} and k_{\perp} wave modes, the spectra at 256³ are approximately converged for $k \leq 20$. As the resolution increases, $\mathcal{P}_u(k)$ extends to higher and higher k -modes, and looks reasonably similar, just with more power at higher k . The correlation scales for each of the $\mathcal{P}_u(k)$ are as follows, MW_1024 $\approx (4.1\ell_{\text{cor},\parallel}, 3.5\ell_{\text{cor},\perp})/\ell_0$, MW_512 $\approx (4.1\ell_{\text{cor},\parallel}, 3.4\ell_{\text{cor},\perp})/\ell_0$, MW_256 = $(4.1\ell_{\text{cor},\parallel}, 3.6\ell_{\text{cor},\perp})/\ell_0$, where $\ell_0 \approx 85$ pc is the measured gaseous scale height.

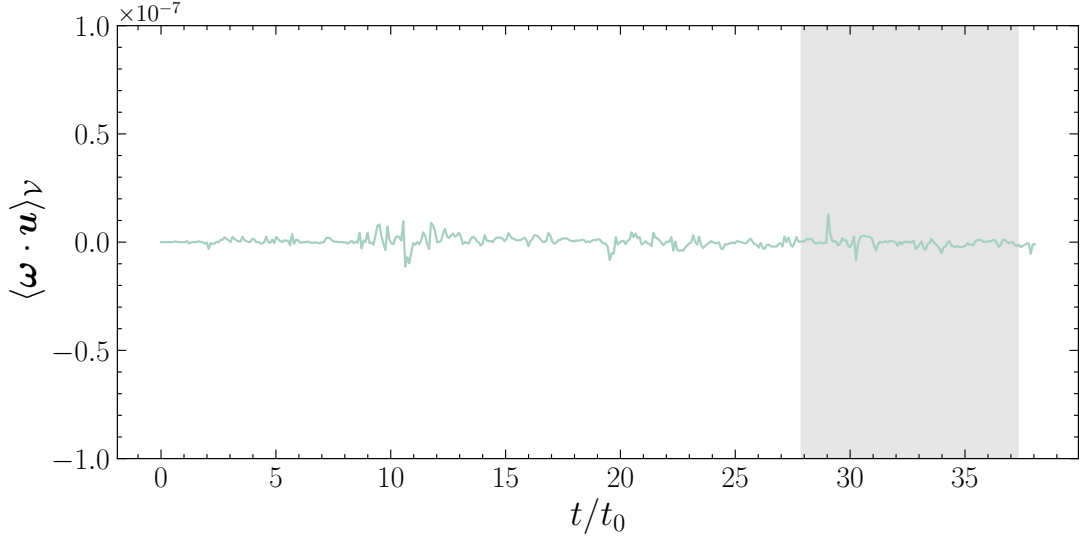


Figure 18. The kinetic helicity, $\mathcal{H}_{\text{kin}} = \langle \boldsymbol{\omega} \cdot \mathbf{u} \rangle_V$, as a function of t/t_0 for the 512^3 simulation, with the gray band showing the stationary state for the supernova-driven turbulence (see Figure 3). Both in the non-stationary and stationary states the turbulence is non-helical to single-precision, $\mathcal{H}_{\text{kin}} \approx 0$, meaning that the inverse transfer that we observe does not require net kinetic helicity. Hence, the inverse cascade we measure in Section 5 is a completely different mechanism compared to homochiral-mediated inverse cascade in 3D turbulence (Plunian et al. 2020).

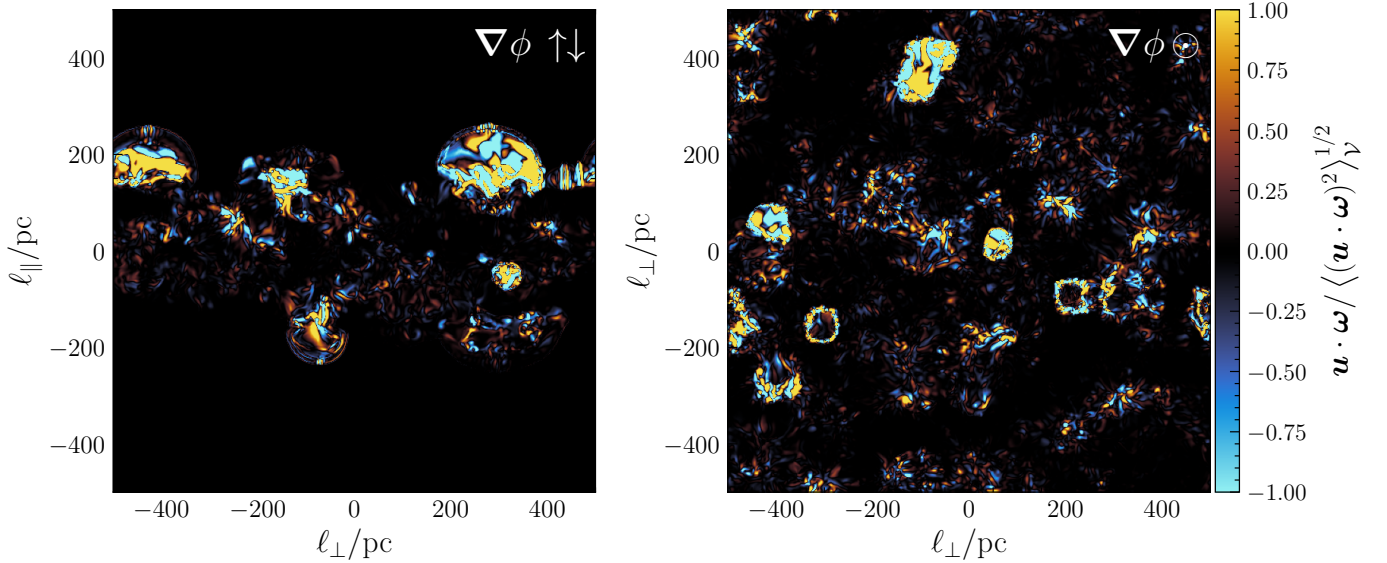


Figure 19. The point-wise kinetic helicity $\boldsymbol{\omega} \cdot \mathbf{u}$ normalized by the rms for a two-dimensional slice along $\nabla\phi$ (left) and perpendicular to $\nabla\phi$ (right). The largest $\boldsymbol{\omega} \cdot \mathbf{u}$ fluctuations, both in amplitude and size scale, trace the expanding remnants, showing how, even in the absence of global shear and with $\mathcal{H}_{\text{kin}} \approx 0$, strong local kinetic helicity fluctuations are generated through detonating SNe.

- Alexakis, A., Mininni, P. D., & Pouquet, A. 2005, *PhRvE*, 72, 046301, doi: [10.1103/PhysRevE.72.046301](https://doi.org/10.1103/PhysRevE.72.046301)
- Armstrong, J. W., Rickett, B. J., & Spangler, S. R. 1995, *The Astrophysical Journal*, 443, 209, doi: [10.1086/175515](https://doi.org/10.1086/175515)
- Bacchini, C., Fraternali, F., Iorio, G., et al. 2020, *A&A*, 641, A70, doi: [10.1051/0004-6361/202038223](https://doi.org/10.1051/0004-6361/202038223)
- Banerjee, S., & Galtier, S. 2017, *Journal of Physics A Mathematical General*, 50, 015501, doi: [10.1088/1751-8113/50/1/015501](https://doi.org/10.1088/1751-8113/50/1/015501)
- Batchelor, G. K. 1959, *Journal of Fluid Mechanics*, 5, 113, doi: [10.1017/S002211205900009X](https://doi.org/10.1017/S002211205900009X)
- Beattie, J. R., Federrath, C., Klessen, R. S., Cielo, S., & Bhattacharjee, A. 2024, arXiv e-prints, arXiv:2405.16626, doi: [10.48550/arXiv.2405.16626](https://doi.org/10.48550/arXiv.2405.16626)

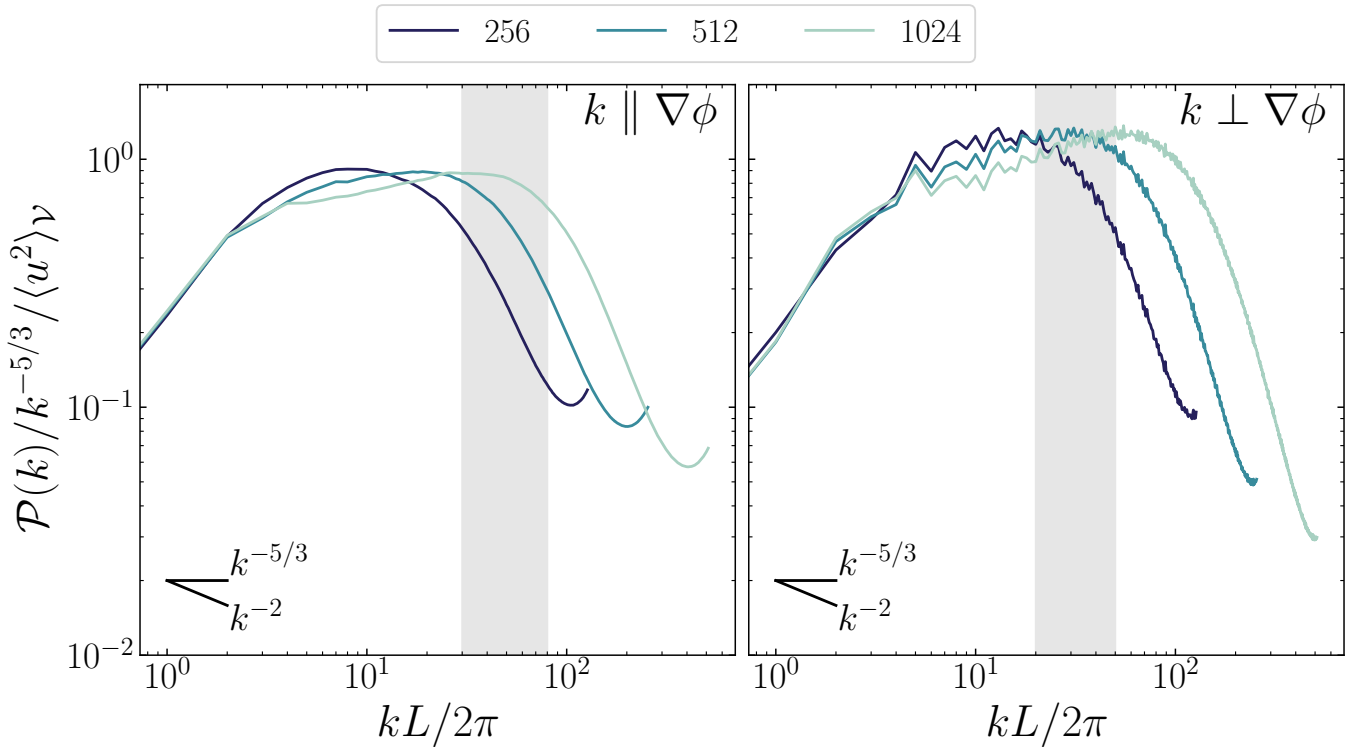


Figure 20. Cylindrically integrated velocity power spectra, $\mathcal{P}_u(k)$, as a function of wavenumbers parallel to the static gravitational potential, Equation 8 ($k_{\parallel} = |k_z|$; left column) and perpendicular to it ($k_{\perp} = \sqrt{k_x^2 + k_y^2}$; right column). Each color represents a different resolution, going from linear resolution $N_{\text{grid}} = 256$ (blue) to $N_{\text{grid}} = 1024$ (light green). We indicate a gray band to show where the cascade is in each spectrum, based on the energy flux results in Section 5. Each spectrum is normalized by the integral square velocity, $\langle u^2 \rangle_{\nu}$ and time-averaged in the stationary regime (see Figure 3) so that intense intermittent events from supernova detonations do not have a strong influence on the spectra.

- Beattie, J. R., Federrath, C., Kriel, N., Hew, J. K. J., & Bhattacharjee, A. 2023a, arXiv e-prints, arXiv:2312.03984, doi: [10.48550/arXiv.2312.03984](https://doi.org/10.48550/arXiv.2312.03984)
- Beattie, J. R., Federrath, C., Kriel, N., Mocz, P., & Seta, A. 2023b, The Monthly Notices of The Royal Astronomical Society, 524, 3201, doi: [10.1093/mnras/stad1863](https://doi.org/10.1093/mnras/stad1863)
- Beattie, J. R., Krumholz, M. R., Federrath, C., Sampson, M. L., & Crocker, R. M. 2022a, Frontiers in Astronomy and Space Sciences, 9, 900900, doi: [10.3389/fspas.2022.900900](https://doi.org/10.3389/fspas.2022.900900)
- Beattie, J. R., Krumholz, M. R., Skalidis, R., et al. 2022b, The Monthly Notices of The Royal Astronomical Society, 515, 5267, doi: [10.1093/mnras/stac2099](https://doi.org/10.1093/mnras/stac2099)
- Beattie, J. R., Mocz, P., Federrath, C., & Klessen, R. S. 2022c, The Monthly Notices of The Royal Astronomical Society, 517, 5003, doi: [10.1093/mnras/stac3005](https://doi.org/10.1093/mnras/stac3005)
- Beck, R., Brandenburg, A., Moss, D., Shukurov, A., & Sokoloff, D. 1996, ARA&A, 34, 155, doi: [10.1146/annurev.astro.34.1.155](https://doi.org/10.1146/annurev.astro.34.1.155)
- Behnel, S., Bradshaw, R., Citro, C., et al. 2011, Computing in Science & Engineering, 13, 31
- Bialy, S., & Burkhart, B. 2020, ApJL, 894, L2, doi: [10.3847/2041-8213/ab8a32](https://doi.org/10.3847/2041-8213/ab8a32)
- Biermann, L. 1950, Zeitschrift Naturforschung Teil A, 5, 65
- Boffetta, G., & Ecke, R. E. 2012, Annual Review of Fluid Mechanics, 44, 427, doi: <https://doi.org/10.1146/annurev-fluid-120710-101240>
- Burgers, J. 1948, Advances in Applied Mechanics, 1, 171, doi: [http://dx.doi.org/10.1016/S0065-2156\(08\)70100-5](http://dx.doi.org/10.1016/S0065-2156(08)70100-5)
- Burkhart, B. 2018, The Astrophysical Journal, 863, 118, doi: [10.3847/1538-4357/aad002](https://doi.org/10.3847/1538-4357/aad002)
- . 2021, PASP, 133, 102001, doi: [10.1088/1538-3873/ac25cf](https://doi.org/10.1088/1538-3873/ac25cf)
- Burkhart, B., Appel, S. M., Bialy, S., et al. 2020, ApJ, 905, 14, doi: [10.3847/1538-4357/abc484](https://doi.org/10.3847/1538-4357/abc484)
- Cernetic, M., Springel, V., Guillet, T., & Pakmor, R. 2024, MNRAS, 534, 1963, doi: [10.1093/mnras/stae2192](https://doi.org/10.1093/mnras/stae2192)
- Chamandy, L., & Shukurov, A. 2020, Galaxies, 8, 56, doi: [10.3390/galaxies8030056](https://doi.org/10.3390/galaxies8030056)
- Childs, H., Brugger, E., Whitlock, B., et al. 2012, in High Performance Visualization—Enabling Extreme-Scale Scientific Insight (Taylor & Francis), 357–372
- Colman, T., Robitaille, J.-F., Hennebelle, P., et al. 2022, MNRAS, 514, 3670, doi: [10.1093/mnras/stac1543](https://doi.org/10.1093/mnras/stac1543)

- Draine, B. T. 2011, *Physics of the Interstellar and Intergalactic Medium*
- Elmegreen, B. G., & Scalo, J. 2004, *ARA&A*, 42, 211, doi: [10.1146/annurev.astro.41.011802.094859](https://doi.org/10.1146/annurev.astro.41.011802.094859)
- Falceta-Gonçalves, D., Kowal, G., Falgarone, E., & Chian, A. C. L. 2014, *Nonlinear Processes in Geophysics*, 21, 587, doi: [10.5194/npg-21-587-2014](https://doi.org/10.5194/npg-21-587-2014)
- Federrath, C. 2013, *The Monthly Notices of The Royal Astronomical Society*, 436, 1245, doi: [10.1093/mnras/stt1644](https://doi.org/10.1093/mnras/stt1644)
- Federrath, C., Chabrier, G., Schober, J., et al. 2011, *Physical Review Letters*, 107, 114504, doi: [10.1103/PhysRevLett.107.114504](https://doi.org/10.1103/PhysRevLett.107.114504)
- Federrath, C., & Klessen, R. S. 2012, *The Astrophysical Journal*, 761, doi: [10.1088/0004-637X/761/2/156](https://doi.org/10.1088/0004-637X/761/2/156)
- Federrath, C., Klessen, R. S., Iapichino, L., & Beattie, J. R. 2021, *Nature Astronomy*, doi: [10.1038/s41550-020-01282-z](https://doi.org/10.1038/s41550-020-01282-z)
- Federrath, C., Roman-Duval, J., Klessen, R., Schmidt, W., & Mac Low, M. M. 2010, *Astronomy and Astrophysics*, 512, doi: [10.1051/0004-6361/200912437](https://doi.org/10.1051/0004-6361/200912437)
- Ferrand, R., Galtier, S., Sahraoui, F., & Federrath, C. 2020, *ApJ*, 904, 160, doi: [10.3847/1538-4357/abb76e](https://doi.org/10.3847/1538-4357/abb76e)
- Ferrière, K. 2020, *Plasma Physics and Controlled Fusion*, 62, 014014, doi: [10.1088/1361-6587/ab49eb](https://doi.org/10.1088/1361-6587/ab49eb)
- Fielding, D. B., Ostriker, E. C., Bryan, G. L., & Jermyn, A. S. 2020, *ApJL*, 894, L24, doi: [10.3847/2041-8213/ab8d2c](https://doi.org/10.3847/2041-8213/ab8d2c)
- Fielding, D. B., Ripperda, B., & Philippov, A. A. 2023, *The Astrophysical Journal Letters*, 949, L5, doi: [10.3847/2041-8213/accflf](https://doi.org/10.3847/2041-8213/accflf)
- Gaensler, B. M., Haverkorn, M., Burkhart, B., et al. 2011, *Nature*, 478, 214, doi: [10.1038/nature10446](https://doi.org/10.1038/nature10446)
- Gent, F. A., Mac Low, M.-M., Käpylä, M. J., & Singh, N. K. 2021, *ApJL*, 910, L15, doi: [10.3847/2041-8213/abed59](https://doi.org/10.3847/2041-8213/abed59)
- Gerrard, I. A., Noon, K. A., Federrath, C., et al. 2024, *MNRAS*, 530, 4317, doi: [10.1093/mnras/stae1144](https://doi.org/10.1093/mnras/stae1144)
- Girichidis, P., Walch, S., Naab, T., et al. 2016, *MNRAS*, 456, 3432, doi: [10.1093/mnras/stv2742](https://doi.org/10.1093/mnras/stv2742)
- Grete, P., O'Shea, B. W., & Beckwith, K. 2020, *The Astrophysical Journal*, 889, 19, doi: [10.3847/1538-4357/ab5aec](https://doi.org/10.3847/1538-4357/ab5aec)
- . 2021, *The Astrophysical Journal*, 909, 148, doi: [10.3847/1538-4357/abdd22](https://doi.org/10.3847/1538-4357/abdd22)
- . 2023, *The Astrophysical Journal Letters*, 942, L34, doi: [10.3847/2041-8213/aca7](https://doi.org/10.3847/2041-8213/aca7)
- Grete, P., O'Shea, B. W., Beckwith, K., Schmidt, W., & Christlieb, A. 2017a, *Physics of Plasmas*, 24, 092311, doi: [10.1063/1.4990613](https://doi.org/10.1063/1.4990613)
- . 2017b, *Physics of Plasmas*, 24, 092311, doi: [10.1063/1.4990613](https://doi.org/10.1063/1.4990613)
- Guo, M., Kim, C.-G., & Stone, J. M. 2024, *arXiv e-prints*, arXiv:2411.12809, doi: [10.48550/arXiv.2411.12809](https://doi.org/10.48550/arXiv.2411.12809)
- Harris, C. R., Millman, K. J., van der Walt, S. J., et al. 2020, *Nature*, 585, 357, doi: [10.1038/s41586-020-2649-2](https://doi.org/10.1038/s41586-020-2649-2)
- Harrison, E. R. 1969, *Nature*, 224, 1089, doi: [10.1038/2241089a0](https://doi.org/10.1038/2241089a0)
- Hennebelle, P., Brucey, N., & Colman, T. 2024, *A&A*, 690, A43, doi: [10.1051/0004-6361/202450524](https://doi.org/10.1051/0004-6361/202450524)
- Hennebelle, P., & Chabrier, G. 2008, *The Astrophysical Journal*, 684, 395, doi: [10.1086/589916](https://doi.org/10.1086/589916)
- Hennebelle, P., & Iffrig, O. 2014, *A&A*, 570, A81, doi: [10.1051/0004-6361/201423392](https://doi.org/10.1051/0004-6361/201423392)
- Hew, J. K. J., & Federrath, C. 2023, *The Monthly Notices of The Royal Astronomical Society*, 520, 6268, doi: [10.1093/mnras/stad545](https://doi.org/10.1093/mnras/stad545)
- Hopkins, P. F., Squire, J., Chan, T. K., et al. 2021, *The Monthly Notices of The Royal Astronomical Society*, 501, 4184, doi: [10.1093/mnras/staa3691](https://doi.org/10.1093/mnras/staa3691)
- Howes, G. G. 2024, *Journal of Plasma Physics*, 90, 905900504, doi: [10.1017/S0022377824001090](https://doi.org/10.1017/S0022377824001090)
- Hu, Y., Lazarian, A., & Xu, S. 2022, *The Monthly Notices of The Royal Astronomical Society*, doi: [10.1093/mnras/stac319](https://doi.org/10.1093/mnras/stac319)
- Hunter, J. D. 2007, *Computing in Science & Engineering*, 9, 90, doi: [10.1109/MCSE.2007.55](https://doi.org/10.1109/MCSE.2007.55)
- Iroshnikov, P. S. 1964, *Soviet Astronomy*, 7, 566
- Joblib Development Team. 2020, *Joblib: running Python functions as pipeline jobs*. <https://joblib.readthedocs.io/>
- Käpylä, M. J., Gent, F. A., Väisälä, M. S., & Sarson, G. R. 2018, *A&A*, 611, A15, doi: [10.1051/0004-6361/201731228](https://doi.org/10.1051/0004-6361/201731228)
- Karpov, P. I., Martizzi, D., Macias, P., et al. 2020, *ApJ*, 896, 66, doi: [10.3847/1538-4357/ab8f23](https://doi.org/10.3847/1538-4357/ab8f23)
- Kempster, P., Fielding, D. B., Quataert, E., et al. 2023, *arXiv e-prints*, arXiv:2304.12335, doi: [10.48550/arXiv.2304.12335](https://doi.org/10.48550/arXiv.2304.12335)
- Kennicutt, Robert C., J. 1998, *ApJ*, 498, 541, doi: [10.1086/305588](https://doi.org/10.1086/305588)
- Kennicutt, Robert C., J., Calzetti, D., Walter, F., et al. 2007, *ApJ*, 671, 333, doi: [10.1086/522300](https://doi.org/10.1086/522300)
- Kim, C.-G., & Ostriker, E. C. 2017, *ApJ*, 846, 133, doi: [10.3847/1538-4357/aa8599](https://doi.org/10.3847/1538-4357/aa8599)
- Klessen, R. S., Heitsch, F., & Mac Low, M.-M. 2000, *The Astrophysical Journal*, 535, 887, doi: [10.1086/308891](https://doi.org/10.1086/308891)
- Kolborg, A. N., Martizzi, D., Ramirez-Ruiz, E., et al. 2022, *ApJL*, 936, L26, doi: [10.3847/2041-8213/ac8c98](https://doi.org/10.3847/2041-8213/ac8c98)
- Kolborg, A. N., Ramirez-Ruiz, E., Martizzi, D., Macias, P., & Soares-Furtado, M. 2023, *ApJ*, 949, 100, doi: [10.3847/1538-4357/acca80](https://doi.org/10.3847/1538-4357/acca80)
- Kolmogorov, A. N. 1941, *Akademiia Nauk SSSR Doklady*, 32, 16
- Kolmogorov, A. N. 1941, *Doklady Akademii Nauk Sssr*, 30, 301, doi: [10.1098/rspa.1991.0075](https://doi.org/10.1098/rspa.1991.0075)
- Kraichnan, R. H. 1965, *The Physics of Fluids*, 8, 1385, doi: [10.1063/1.1761412](https://doi.org/10.1063/1.1761412)
- Kraichnan, R. H. 1967, *Physics of Fluids*, 10, 1417, doi: [10.1063/1.1762301](https://doi.org/10.1063/1.1762301)
- Kraichnan, R. H. 1971, *Journal of Fluid Mechanics*, 47, 525–535, doi: [10.1017/S0022112071001216](https://doi.org/10.1017/S0022112071001216)
- Kriel, N., Beattie, J. R., Federrath, C., Krumholz, M. R., & Hew, J. K. J. 2023, *arXiv e-prints*, arXiv:2310.17036, doi: [10.48550/arXiv.2310.17036](https://doi.org/10.48550/arXiv.2310.17036)
- Kriel, N., Beattie, J. R., Seta, A., & Federrath, C. 2022, *The Monthly Notices of The Royal Astronomical Society*, 513, 2457, doi: [10.1093/mnras/stac969](https://doi.org/10.1093/mnras/stac969)

- Krumholz, M. R. 2015, ArXiv e-prints, arXiv:1511.03457. <https://arxiv.org/abs/1511.03457>
- Krumholz, M. R., & Burkhardt, B. 2016, MNRAS, 458, 1671, doi: [10.1093/mnras/stw434](https://doi.org/10.1093/mnras/stw434)
- Krumholz, M. R., & McKee, C. F. 2005, The Astrophysical Journal, 630, 250, doi: [10.1086/431734](https://doi.org/10.1086/431734)
- Krumholz, M. R., & Ting, Y.-S. 2018, The Monthly Notices of The Royal Astronomical Society, 475, 2236, doi: [10.1093/mnras/stx3286](https://doi.org/10.1093/mnras/stx3286)
- Kuijken, K., & Gilmore, G. 1989, MNRAS, 239, 605, doi: [10.1093/mnras/239.2.605](https://doi.org/10.1093/mnras/239.2.605)
- Kulsrud, R. M., Cen, R., Ostriker, J. P., & Ryu, D. 1997, ApJ, 480, 481, doi: [10.1086/303987](https://doi.org/10.1086/303987)
- Lam, S. K., Pitrou, A., & Seibert, S. 2015, in Proc. Second Workshop on the LLVM Compiler Infrastructure in HPC, 1–6, doi: [10.1145/2833157.2833162](https://doi.org/10.1145/2833157.2833162)
- Lancaster, L., Ostriker, E. C., Kim, C.-G., Kim, J.-G., & Bryan, G. L. 2024, ApJ, 970, 18, doi: [10.3847/1538-4357/ad47f6](https://doi.org/10.3847/1538-4357/ad47f6)
- Lancaster, L., Ostriker, E. C., Kim, J.-G., & Kim, C.-G. 2021, ApJ, 914, 89, doi: [10.3847/1538-4357/abf8ab](https://doi.org/10.3847/1538-4357/abf8ab)
- Li, M., Li, Y., Bryan, G. L., Ostriker, E. C., & Quataert, E. 2020, ApJ, 898, 23, doi: [10.3847/1538-4357/ab9c22](https://doi.org/10.3847/1538-4357/ab9c22)
- Lithwick, Y., & Goldreich, P. 2001, The Astrophysical Journal, 562, 279, doi: [10.1086/323470](https://doi.org/10.1086/323470)
- Mac Low, M.-M. 1999, The Astrophysical Journal, 524, 169, doi: [10.1086/307784](https://doi.org/10.1086/307784)
- Maffioli, A. 2017, Physical Review Fluids, 2, 104802, doi: [10.1103/PhysRevFluids.2.104802](https://doi.org/10.1103/PhysRevFluids.2.104802)
- Malvadi Shivakumar, L., & Federrath, C. 2023, arXiv e-prints, arXiv:2311.10350, doi: [10.48550/arXiv.2311.10350](https://doi.org/10.48550/arXiv.2311.10350)
- Martizzi, D., Faucher-Giguère, C.-A., & Quataert, E. 2015, MNRAS, 450, 504, doi: [10.1093/mnras/stv562](https://doi.org/10.1093/mnras/stv562)
- Martizzi, D., Fielding, D., Faucher-Giguère, C.-A., & Quataert, E. 2016, MNRAS, 459, 2311, doi: [10.1093/mnras/stw745](https://doi.org/10.1093/mnras/stw745)
- Mathew, S. S., Federrath, C., & Seta, A. 2023, MNRAS, 518, 5190, doi: [10.1093/mnras/stac3415](https://doi.org/10.1093/mnras/stac3415)
- McKee, C. F., & Ostriker, J. P. 1977, ApJ, 218, 148, doi: [10.1086/155667](https://doi.org/10.1086/155667)
- McKee, C. F., Parravano, A., & Hollenbach, D. J. 2015, ApJ, 814, 13, doi: [10.1088/0004-637X/814/1/13](https://doi.org/10.1088/0004-637X/814/1/13)
- McKee, C. F., Stacy, A., & Li, P. S. 2020, The Monthly Notices of The Royal Astronomical Society, 496, 5528, doi: [10.1093/mnras/staa1903](https://doi.org/10.1093/mnras/staa1903)
- Mininni, P., Alexakis, A., & Pouquet, A. 2005, PhRvE, 72, 046302, doi: [10.1103/PhysRevE.72.046302](https://doi.org/10.1103/PhysRevE.72.046302)
- Mohapatra, R., Federrath, C., & Sharma, P. 2022, MNRAS, 514, 3139, doi: [10.1093/mnras/stac1610](https://doi.org/10.1093/mnras/stac1610)
- Mohapatra, R., & Quataert, E. 2024, ApJ, 965, 105, doi: [10.3847/1538-4357/ad2940](https://doi.org/10.3847/1538-4357/ad2940)
- Monin, A. S., & Iaglom, A. M. 1975, Statistical fluid mechanics: Mechanics of turbulence. Volume 2 /revised and enlarged edition/
- Nam, D. G., Federrath, C., & Krumholz, M. R. 2021, The Monthly Notices of The Royal Astronomical Society, 503, 1138, doi: [10.1093/mnras/stab505](https://doi.org/10.1093/mnras/stab505)
- Nandakumar, M., & Dutta, P. 2023, MNRAS, 526, 4690, doi: [10.1093/mnras/stad3042](https://doi.org/10.1093/mnras/stad3042)
- Nazarenko, S. V., & Schekochihin, A. A. 2011, Journal of Fluid Mechanics, 677, 134, doi: [10.1017/S002211201100067X](https://doi.org/10.1017/S002211201100067X)
- Oliphant, T. 2006, NumPy: A guide to NumPy, USA: Trelgol Publishing. <http://www.numpy.org/>
- Padoan, P., Pan, L., Haugbølle, T., & Nordlund, Å. 2016, The Astrophysical Journal, 822, 11, doi: [10.3847/0004-637X/822/1/11](https://doi.org/10.3847/0004-637X/822/1/11)
- Pan, L., Padoan, P., Haugbølle, T., & Nordlund, Å. 2016, ApJ, 825, 30, doi: [10.3847/0004-637X/825/1/30](https://doi.org/10.3847/0004-637X/825/1/30)
- pandas development team, T. 2023, pandas-dev/pandas: Pandas, 2.1.4, Zenodo, doi: [10.5281/zenodo.10304236](https://doi.org/10.5281/zenodo.10304236)
- Plunian, F., Teimurazov, A., Stepanov, R., & Verma, M. K. 2020, Journal of Fluid Mechanics, 895, A13, doi: [10.1017/jfm.2020.307](https://doi.org/10.1017/jfm.2020.307)
- Rincon, F. 2019, Journal of Plasma Physics, 85, 205850401, doi: [10.1017/S0022377819000539](https://doi.org/10.1017/S0022377819000539)
- Schekochihin, A. A., Cowley, S. C., Hammett, G. W., Maron, J. L., & McWilliams, J. C. 2002, New Journal of Physics, 4, 84, doi: [10.1088/1367-2630/4/1/384](https://doi.org/10.1088/1367-2630/4/1/384)
- Schekochihin, A. A., Cowley, S. C., Taylor, S. F., Maron, J. L., & McWilliams, J. C. 2004, The Astrophysical Journal, 612, 276, doi: [10.1086/422547](https://doi.org/10.1086/422547)
- Schober, J., Schleicher, D., Federrath, C., Klessen, R., & Banerjee, R. 2012, PhRvE, 85, 026303, doi: [10.1103/PhysRevE.85.026303](https://doi.org/10.1103/PhysRevE.85.026303)
- Schober, J., Schleicher, D. R. G., Federrath, C., Bovino, S., & Klessen, R. S. 2015, Physical Review E, 92, 023010, doi: [10.1103/PhysRevE.92.023010](https://doi.org/10.1103/PhysRevE.92.023010)
- Schumacher, J., Scheel, J. D., Krasnov, D., et al. 2014, Proceedings of the National Academy of Sciences, 111, 10961, doi: [10.1073/pnas.1410791111](https://doi.org/10.1073/pnas.1410791111)
- Seta, A., & Federrath, C. 2022, The Monthly Notices of The Royal Astronomical Society, 514, 957, doi: [10.1093/mnras/stac1400](https://doi.org/10.1093/mnras/stac1400)
- Sharda, P., Ginzburg, O., Krumholz, M. R., et al. 2024, MNRAS, 528, 2232, doi: [10.1093/mnras/stae088](https://doi.org/10.1093/mnras/stae088)
- Stone, J. M., Ostriker, E. C., & Gammie, C. F. 1998, The Astrophysical Journal Letters, 508, L99, doi: [10.1086/311718](https://doi.org/10.1086/311718)
- Stroustrup, B. 2013, The C++ Programming Language, 4th edn. (Addison-Wesley Professional)
- Sutherland, R. S., & Dopita, M. A. 1993, ApJS, 88, 253, doi: [10.1086/191823](https://doi.org/10.1086/191823)
- Tevlin, L., Berlok, T., Pfrommer, C., et al. 2024, arXiv e-prints, arXiv:2411.00103, doi: [10.48550/arXiv.2411.00103](https://doi.org/10.48550/arXiv.2411.00103)
- Teyssier, R. 2002, A&A, 385, 337, doi: [10.1051/0004-6361:20011817](https://doi.org/10.1051/0004-6361:20011817)
- Theuns, T., Leonard, A., Efstathiou, G., Pearce, F. R., & Thomas, P. A. 1998, MNRAS, 301, 478, doi: [10.1046/j.1365-8711.1998.02040.x](https://doi.org/10.1046/j.1365-8711.1998.02040.x)
- Thompson, C. 2023, MNRAS, 519, 497, doi: [10.1093/mnras/stac3565](https://doi.org/10.1093/mnras/stac3565)

- Turk, M. J., Smith, B. D., Oishi, J. S., et al. 2011, *ApJS*, 192, 9, doi: [10.1088/0067-0049/192/1/9](https://doi.org/10.1088/0067-0049/192/1/9)
- van der Velden, E. 2020, *The Journal of Open Source Software*, 5, 2004, doi: [10.21105/joss.02004](https://doi.org/10.21105/joss.02004)
- van der Walt, S., Schönberger, J. L., Nunez-Iglesias, J., et al. 2014, *PeerJ*, 2, e453, doi: [10.7717/peerj.453](https://doi.org/10.7717/peerj.453)
- Virtanen, P., Gommers, R., Oliphant, T. E., et al. 2020, *Nature Methods*, 17, 261, doi: <https://doi.org/10.1038/s41592-019-0686-2>
- Waleffe, F. 1992, *Physics of Fluids A: Fluid Dynamics*, 4, 350, doi: [10.1063/1.858309](https://doi.org/10.1063/1.858309)
- Wolfire, M. G., Hollenbach, D., McKee, C. F., Tielens, A. G. G. M., & Bakes, E. L. O. 1995, *The Astrophysical Journal*, 443, 152, doi: [10.1086/175510](https://doi.org/10.1086/175510)
- Xu, S., & Lazarian, A. 2016, *The Astrophysical Journal*, 833, 215, doi: [10.3847/1538-4357/833/2/215](https://doi.org/10.3847/1538-4357/833/2/215)
- Zweibel, E. 2013, *Physics Online Journal*, 6, 85, doi: [10.1103/Physics.6.85](https://doi.org/10.1103/Physics.6.85)